An experimental investigation of dyke injection under regional extensional stress

Katherine A. Daniels, Thierry Menand

An experimental investigation of dyke injection under regional extensional stress.

K. A. Daniels[1,2] and T. Menand[3].

[1]Department of Earth Sciences, University of Cambridge, Downing Street, Cambridge, CB2 3EQ.

[2]School of Earth Sciences, University of Bristol, Wills Memorial Building, Queen's Road, Bristol, BS8 1RJ, U.K.

[3]Laboratoire Magmas et Volcans, Université Blaise Pascal – CNRS – IRD, OPGC, 5 rue Kessler, 63038, Clermont-Ferrand, France.

ABSTRACT

Dyke injection is a fundamental process of magma transport in the crust, occurring in all tectonic settings. The effect of extensional stress regimes on dyke injections is particularly important to understanding a wide spectrum of processes including continental rifting and volcanic activity. Yet, dyke injection in extensional regimes has been relatively understudied. In addition, the effect of dyke-dyke interaction modifying the surrounding stress field and leading to dyke rotation about the vertical axis has not been addressed. We present the results from 23 laboratory analogue experiments investigating lateral dyke injections in a remote extensional stress field. This study is unique in that it addresses the effect of both extension and dyke-dyke interaction on the lateral propagation and rotation of dykes. The experiments study the interrelationship between successive lateral dyke injections by examining dyke injection thickness,

injection spacing, injection orientation, extension and structural relationship. A relationship between the rotation angle between two successive intrusions and the distance separating them under given extensional stress conditions is established. The rotation angle depends on two dimensionless numbers: the ratio of fluid overpressure of the first injection and remote tensile stress, and the ratio of the spacing between injections and the height of the first intrusion. The experiments show how the stress field is perturbed by an intrusion, and how the remote stress field is locally relieved by this intrusion. The results show furthermore that measuring or estimating the rotation angles between successive intrusions within rift zones allows the spatial distribution of these intrusions to be estimated. In the case of the actively spreading Red Sea rift in Afar, Ethiopia, we find that the vast majority of the dykes are predicted to intrude within 10 km of each other, and most frequently between 4 and 5 km, in good agreement with independent geophysical observations.

INTRODUCTION

Dyke injection is a fundamental process of magma transport in the crust. Extension of the crust can be accommodated both tectonically, through brittle failure, and by magma injection in dykes. During continental rifting (Maguire et al., 2006; White et al., 2008; Thybo and Nielsen, 2009; Daniels et al., 2014) extension through dyke injection requires lower yield stresses than mechanical extension through faulting or for stretching of a thick continental lithosphere (e.g., Buck, 2004; 2006; Bialas et al., 2010). Dyke injection however occurs in many tectonic settings including at hot spot volcanoes

(e.g. Fiske and Jackson, 1972) and arcs (e.g. Wadge, 1986), and extension can occur locally in these regions. Therefore the effect of an extensional stress regime on dyke injection is of importance to magma transport to volcanoes in all tectonic settings. Extension could also help in focusing repeated dyke injections but whether and how this would occur precisely remains unclear.

A dyke's orientation will change as it enters a new stress regime (e.g. Menand et al., 2010). Similarly, a dyke injection will modify the tectonic stress of the host material on a local scale (e.g. Reches and Fink, 1988). For instance, many en echelon dykes have segments that exhibit a teardrop, asymmetrical shape, their widest part being at one of their tips and with neighbouring segments displaying this asymmetry in alternating directions. This is attributed to the stresses associated with the simultaneous intrusion of neighbouring dyke segments that overlap (Daniels et al., 2012) and provides field evidence that one dyke injection can influence the propagation or orientation of another. In the case of successive dyke injections, rotation of the orientation of a second dyke will occur in comparison with the first, provided the first dyke has sufficiently altered the stress regime, and so the proximity of dykes to one another can act to focus subsequent dykes into the same region (Ito and Martel 2002). Indeed, the regional stress field can be perturbed on a local scale by high rates of magma supply (Paquet et al., 2007).

In extensional tectonic settings, the rotation of dykes about their vertical axis has been observed in association with intrusions at spreading centres, especially at sites of transform faults, where the extensional stresses are not uniform (e.g. MacLeod et al., 1990; Dietrich and Spencer, 1993). As an example, previous workers have used the Troodos Ophiolite in Cyprus as an analogue for mid ocean ridge spreading, studying the

Sheeted Dyke Complex, Southern Troodos Transform Fault Zone (STTFZ) (Dietrich and Spencer, 1993, and references therein) and the Solea Graben (thought to be a fossil ridge axis; Varga and Moores, 1985). Many dykes in the northern part of the Troodos Ophiolite demonstrate a rotation in their orientation about their vertical axis from a north-south strike to an east-west one, as they approach transform fault zones. The rotation of these dykes has been attributed either to the stress field changes associated with a strike-slip transform fault (Varga and Moores, 1985; Murton, 1986; Moores et al., 1990; Dilek et al., 1990), or a physical rotation due to fault drag on large blocks in the fault zone (Bonhommet et al., 1988; Allerton, 1989; Allerton and Vine, 1991), although palaeomagnetic studies of the initial magnetisation of the dykes during cooling showing a rotation magnetisation supports the second explanation. However, it is likely that the dyke rotation during the formation of the oceanic crust at Troodos happened at an early stage (MacLeod et al., 1990). Dyke rotation at other rift settings has also been observed (Figure 1); ground deformation modelling from INSAR data measured during the Afar rifting episode, Afar Ethiopia, estimated a range of up to 16^{o} between the different dykes' strikes of that episode (Hamling et al., 2009; Hamling et al., 2010; Ebinger et al., 2010). A key aspect of rift settings is that it usually involves repeated lateral dyke intrusions. For instance, lateral dyke propagation away from rift-axial volcanoes and magma chambers has been observed both in Iceland during the 1975-1984 Krafla rifting episode (e.g. Brandsdottir and Einarsson, 1979) and on the Manda Hararo-Dabbahu rift segment of the Red Sea Rift (e.g. Wright et al., 2006; Keir et al., 2009; Keir et al., 2011) (Figure 1C). Also, the stress changes that are induced by a dyke injection in a rift can have a strong effect in determining the location of subsequent magma injections

(Hamling et al., 2010). However, to our knowledge, this effect has not been fully quantified, and in particular the arrangement of successive dykes in both space and time.

FIGURE 1 (FIGURE1_DykeSetting5.pdf)

Numerous scaled analogue experimental models have been used to study various aspects of dyke injection and propagation (e.g. Heimpel and Olson, 1994; Takada, 1994a; Menand and Tait, 2001; Menand and Tait, 2002; Kavanagh et al., 2006; Menand, 2008; Menand et al., 2010; Taisne and Tait, 2009; Taisne and Tait, 2011), including buoyancy-driven fracture propagation (Fiske and Jackson, 1972; Maaloe, 1987; Takada, 1990; Heimpel and Olson, 1994; Rivalta et al., 2005) and the interaction of vertically propagating fluid-filled cracks (Takada, 1994b; Ito and Martel, 2002; Watanabe et al., 2002). Lateral spreading of dyke injections as the result of rigidity contrasts or the lack of a density difference (where buoyancy pressures are insignificant (Rubin and Pollard, 1987; Ryan, 1987; Lister and Kerr, 1991; Taisne and Jaupart, 2009)) may also generate volcanic rift zones (Heimpel and Olson, 1994). Takada (1994), Ito and Martel (2002), as well as Watanabe et al. (2002) showed that the local stress field is distorted by an intruding dyke, and that this distortion will alter the path of a second dyke. Ito and Martel (2002) also showed that multiple dykes could be focussed beneath mid-ocean ridges as a consequence of the injection of previous dykes. Kühn and Dahm (2004; 2008) showed that the trade-off between magma pressure and deviatoric stress gradient controls whether magma intrusion results in the formation of vertical sheeted dykes or a magma chamber from stacked sills. Menand et al. (2010) used buoyant injections to show that vertical dykes entering a horizontal

compressional tectonic stress field will rotate towards the direction of maximum compressive stress, i.e. a horizontal plane, and therefore form a sill, if the compressive stresses are large compared to the dyke buoyancy. In addition, Le Corvec and co-workers (2013) demonstrated the influence of an extensional stress regime and the presence of pre-existing fractures on the propagation paths of dykes. They found that pre-existing fractures could control both the direction and speed of propagation of a dyke, especially if the dyke volume was small or there were multiple fractures. The propagation path of a dyke is thus controlled by the stresses acting on the region that the dyke is propagating through (e.g. Gudmundsson, 2006; Menand et al., 2010). As illustrated by these previous studies, analogue experimental models provide a method for determining the effect of multiple dyke injection on the regional stress and the cumulative effect of multiple injections in an originally extensional stress. However, whilst laboratory experiments have been conducted to make comparisons with a number of different geological settings, few involved the injection of an analogue magma fluid into a solid in extension (e.g. Walter and Troll, 2003; Le Corvec et al., 2013). Furthermore, to our knowledge, there have been no experimental studies that investigate the effect of repeated injections in an extensional environment, and their subsequent arrangement in both space and time.

We present the results from a series of 23 laboratory analogue experiments which involved the repeated injection of a magma analogue (vegetable oil) into an analogue crust (gelatine) subjected to a remote extension. This study is unique in that it addresses the effect of both extension and dyke-dyke interaction on the lateral propagation of dykes. The study uses sequential dyke intrusions to understand how

dykes modify the strain in the material surrounding them and alter the behaviour of the next dyke. These experiments were designed to investigate, from a structural point of view, the relationship between successive laterally propagating dykes injected in an extensional tectonic setting, relating dyke injection size, amount of extension, injection spacing and injection orientation.

EXPERIMENTAL SET-UP, MATERIALS AND METHOD

As a transparent, elastic solid, gelatine is commonly used as a crustal analogue for modelling magmatic intrusions (e.g. Johnson and Pollard, 1973; Pollard and Johnson, 1973; Takada, 1990; Takada, 1994a; Takada, 1994b; Heimpel and Olson, 1994; Dahm, 2000b; Menand and Tait, 2001; Menand and Tait, 2002; Ito and Martel, 2002; Watanabe et al., 2002; Rivalta et al., 2005; Kavanagh et al., 2006; Menand, 2008; Menand et al., 2010; Kavanagh et al., 2013), although granular materials have also successfully been used to model the crust (e.g. Galland et al., 2006; Mathieu et al., 2008; Galland et al. 2009; Kervyn et al., 2009; Galerne et al. 2011). The advantage of using gelatine however is that the visualisation of the dyke propagation is possible. Experimental magma analogues have been more varied and include water (e.g. Kavanagh et al., 2006); air (e.g. Menand et al., 2010); oils (e.g. Heimpel and Olson, 1994; Takada, 1994a; Galland et al., 2006); hydroxyethylcellulose solutions (e.g. Menand and Tait, 2001); and Hexane or Mercury (e.g. Heimpel and Olson, 1994).

Gelatine and its preparation

Gelatine is a homogenous, isotropic, and transparent, brittle viscoelastic solid, and is incompressible to the degree that its Poisson's ratio can be taken as 0.5 (Farquharson

and Hennes, 1940; Crisp, 1952; Richards and Mark, 1966; Righetti et al., 2004; Kavanagh et al., 2013). As shown by Kavanagh et al. (2013), gelatine can be tailored to be an appropriate laboratory-scale analogue material to model the intrusion of magma in the elastic, brittle crust, provided that low temperatures, stresses, and strains, as well as concentrations in the range 2-5 wt.% are used.

Each experiment presented here comprised a two-layered gelatine block prepared in a Perspex tank. The upper layer was more rigid than the lower one to prevent experimental dykes from reaching the surface and thus forcing instead their lateral propagation within the lower layer. This technique enabled us to generate the lateral propagation of the fluid intrusions. Analysis of the experiments requires knowledge of the lower layer gelatine Young's modulus once solid. The usual method for determining the Young's modulus of a gelatine solid is to measure the vertical deflection of the gelatine upper surface created by a load of known magnitude and geometry: a digital micrometre screw gauge is used to calculate the distance between a fixed point and the surface of the gelatine, a cylindrical load is applied to the surface of the gelatine, and the distance between the fixed point and the surface of the gelatine deflected by the load is measured as precisely as possible. Assuming the gelatine is a semi-infinite elastic solid, the Young's modulus can be calculated using

$$E = \frac{mg(1-\nu^2)}{2\,r\,D} \quad (1)$$

where m is the mass of the load, g is 9.81 m/s^2, ν is the Poisson's ratio, r is the radius of the load and D is the deformation of the gelatine due to the load (Timoshenko and Goodier, 1970). Provided the size of the load is less than 10% that of the gelatine solid,

tank-wall effects are negligible. However, this technique requires direct access to the upper free surface of the layer whose Young's modulus is to be measured. In our two-layer gelatine solid, the lower layer is inaccessible. This difficulty was circumvented by preparing two batches of the lower layer of identical volumes and poured in two identical tanks: the experimental tank, used for the experiments, and a control tank, used to measure the Young's modulus of the lower layer.

The gelatine was prepared from a high-clarity, 260 bloom, pigskin-derived, granular powder dissolved in hot, de-ionised water. A 2-wt. % aqueous solution was prepared initially and transferred in equal amounts of 29 L into the two identical acrylic tanks with internal dimensions of 40.0 by 39.8 by 28.9 cm. Both tanks were covered by wrapping film and situated in a cold room with a temperature of 4^{o}C for between 12 and 18 hours, allowing the gelatine to cure, whilst preventing the gelatine forming a tough skin. Subsequently, a further 10 L mixture of 5-wt.%-solution gelatine was then prepared and added only to the experimental tank as the upper layer before returning this tank to the cold room with the control tank for another 6 to 12 hours (Figure 2 A). The gelatine solidification time, temperature, layer volumes and concentrations were recorded (Table 1). The gelatine concentrations, curing temperatures and times ensured that the experiments were correctly scaled to investigate natural magmatic intrusions in terms of geometry, kinematics and dynamics (Kavanagh et al., 2013).

FIGURE 2 (FIGURE2_LABexpApparatusSETUP2.pdf)

Once the gelatine in the experimental tank was solid, the Young's modulus of the gelatine in the control tank was measured using the method described above (Table 1),

202 and the measured value was assumed to be equal to the Young's modulus value of the
203 lower layer in the experimental tank. This was done for each experiment. The
204 experimental tank was then removed from the cold room to run an experiment at room
205 temperature, which allowed a better temperature control of the injected hot analogue
206 fluid. The experiment was sufficiently fast to assume that the mechanical properties of
207 the gelatine solid did not change during the experiment.

208 Extensional stress field

209 A uniform remote tectonic extension was simulated by vertically compressing the
210 gelatine solid and allowing it to respond by deforming horizontally as detailed in Le
211 Corvec et al. (2013) (Figure 2C and D). Removable copper and aluminium plates
212 (dimensions: 39.5 by 32.4 by 1.25 cm) lined two opposite tank walls. After the Young's
213 modulus measurement, these metal plates were heated by circulating hot water within
214 them, removed and the space vacated by the plates was filled with water, whose
215 density is close to that of solid gelatine. The remaining two sides and base of the
216 gelatine were separated from the tank walls with a square U-shaped slice, which had
217 the dimensions of the gelatine solid. Therefore, the boundary conditions for the gelatine
218 solid were a zero shear stress boundary condition with a non-zero hydrostatic pressure
219 pushing on the two gelatine walls initially in contact with the metal plates, and a free-slip
220 boundary condition (no normal displacement) for the other walls of the gelatine solid
221 and its base (Figure 2B and C). After each injection the zero shear stress boundaries
222 moved closer to the edges of the tank, by less than 1 mm, increasing the height of the
223 water level at the sides of the tank by approximately the same amount. This changed
224 the hydrostatic pressure pushing on the gelatine by a few Pa only, which was thus

neglected. The extension (in the x-direction) was generated by applying a uniform load to the gelatine's top surface (and compressing in the z-direction) until the sides of the gelatine had extended by the required amount (Figure 2D, Table 1). This technique allowed the unconfined pair of gelatine walls to extend freely and ensured a uniform stress within the gelatine solid. The amount of induced extension ΔL was varied between experiments, and the stress field in the x, y and z directions generated due to this extension was then calculated (see Appendix for details):

$$\sigma_x = -\frac{4}{3} E \frac{\Delta L}{L} \quad (2)$$

$$\sigma_y = -\frac{2}{3} E \frac{\Delta L}{L} \quad (3)$$

$$\sigma_z = 0 \quad (4)$$

where L is the original gelatine horizontal length, ΔL is the induced horizontal extension and E is the Young's modulus. The stress conditions for each experiment are listed in Table 1.

Analogue fluid properties and injection conditions

The experiments involved the repeated injection of fluid in the gelatine solids to create experimental dykes. Dykes were injected into a pristine gelatine block. A small slit (approximately 1 cm by 2 cm) was initially cut into the gelatine perpendicular to the extension direction, and a tapered injection nozzle was carefully oriented to initiate the injections and feed the fluid into this slit. This technique ensured the formation of experimental dykes that were initially oriented perpendicular to the direction of

extension in the gelatine (parallel to σ_1 and perpendicular to σ_3), rose quickly to the interface between the two gelatine layers and then spread more slowly in a lateral direction. For the first dyke, after the fluid had reached the interface and begun propagating laterally, the propagation speed of the crack tips at either end of the dyke slowed down so that each tip was propagating at roughly half the speed of the crack tip rising vertically. The propagation speed of the subsequent dykes was slower than for the first dykes, and the rise speed was comparable to the lateral propagation speed. The total time taken to conduct all of the injections in an experiment was always less than 1 hour, with the duration of the majority being close to 20 minutes. Once the dyke had moved away from the injection point, the stress field in the gelatine controlled its orientation. To prevent the coalescence of successive fluid injections and to preserve the structural relationship between the successive dykes, a solidifying analogue injection fluid was used. This fluid was a vegetable oil under the Trade name Vegetaline that has previously been used as a magma analogue (Galland et al., 2003; 2006; 2007; 2008; 2009; Chanceaux and Menand, 2014). Vegetaline also has a well-established viscosity-temperature relationship due to the rheological testing presented in Galland et al., (2006). The melting point (31^{o}C) is at an easy temperature to work with under laboratory conditions, and allows the extraction of the solidified dykes from the gelatine for further analysis, after the completion of each experiment.

If solidification occurs during dyke propagation, segmentation and fingering of the dyke edges (e.g. Rubin, 1995) can occur, producing dyke shapes that are harder to analyse in terms of the stresses they impose on their surroundings. Alternatively, the injection of a fluid that is too hot could cause the gelatine in contact with the fluid to melt during the

experiment, affecting the accurate measurement of the stresses generated by the injection. Taisne and Tait (2011) investigated the propagation of a solidifying dyke of parafin wax into a homogenous block of gelatine and defined two dimensionless parameters to predict when solidification or melting is expected to occur, the dimensionless flux (Φ) and the dimensionless temperature (Θ) (See Taisne and Tait, 2011 for further details).

The dimensionless flux represents the dynamical conditions of the injection and is the ratio of the advected heat flux due to the flow into the fissure to the heat lost due to conduction within the gelatine (Taisne and Tait, 2011). The dimensionless temperature represents the injection's thermal conditions and is the ratio of the difference between the Vegetaline phase-change temperature (Ts) and the ambient temperature of the gelatine solid host (T_∞), to the difference between the Vegetaline fluid injection temperature and the solid gelatine temperature. Values for Θ can range between 0 and 1. The larger the Θ value, the lower the injection temperature and the smaller the difference between the injection temperature and the gelatine temperature. Thus, larger Θ values correspond to thermal conditions closer to solidification. Conversely, low values of dimensionless temperature ($\Theta \rightarrow 0$) correspond to thermal conditions far from solidification. Consequently, high injection temperatures ($\Theta \rightarrow 0$) cause a smooth and gradual propagation of the injected dyke. As the injection temperature approaches the solidification temperature ($\Theta \rightarrow 1$), cooling and solidification increase and dyke propagation becomes stepwise (Taisne and Tait, 2011). For a natural system, Θ should be between 0.9 and 0.95 because in most cases, magmas are injected close to their liquidus temperature (Delaney and Pollard, 1982; Taisne and Tait, 2011). Theoretically,

Φ can range between 0 and ∞; everything else being equal, a larger Φ value corresponds to a larger volumetric flux and therefore a faster injection rate. Slow injection rates ($\Phi \rightarrow$ zero) promote solidification, whilst faster injection rates where $\Phi >> 1$ produce almost no solidification (Taisne and Tait 2011, Chanceaux and Menand 2014). The dimensionless flux and temperature are related according to

$$\alpha = \Theta^{\frac{5.36}{\Phi}} \quad (5)$$

the value of which (Figure 3) can be used to describe the solidification characteristics of the dyke injection (Taisne and Tait, 2011). α is always between 0 and 1; if α close to 1 solidification dominates (if α = 1 no propagation would take place as the injection would immediately freeze) and induces an intermittent stepwise propagation of the experimental dyke with a discontinuous and jagged geometry. If α = 0 there is no solidification and propagation is continuous with a smooth dyke geometry. However, α values very close to zero correspond to hotter fluid injections that may melt the gelatine solid. Therefore a threshold maximum value of α = 0.5 was arbitrarily set to ensure that a solidification-induced jagged geometry (α close to 1) did not occur during the experiments. Moreover, when melting of the gelatine solid happened, owing to too small an α value, this generally occurred close to the injector and generated small immiscible bubbles of molten gelatine that were picked up by the injected fluids. This melting could thus be identified after the experiments by the presence of thermally eroded gelatine around the injector and the solidified gelatine bubbles. Experiments that displayed such melting evidence were removed from our analysis.

FIGURE 3 (FIGURE3_NEWalpha1707143.pdf)

309 During each experiment, the fluid was injected using a peristaltic pump at a constant
310 volumetric flux, and the temperature of the fluid at the injection point was maintained
311 constant; the injections continued to propagate, driven by their buoyancy, for a short
312 time (on the order of 0.5 min) after the pump had been switched off. The volumetric flux
313 and temperature for each experiment were chosen so that the corresponding Φ and Θ
314 values of each experiment gave α values that were consistently below 0.5 (the bold line
315 in Figure 3); to obtain these values, the vegetable oil temperature and volumetric flux
316 were kept within specific ranges (40 – 60^{o}C and 59.78 to 179.35 ml/min respectively).

317 Variable volume intrusions of the buoyant fluid were injected at a constant flux into the
318 underlying gelatine layer through small holes in the base of the tank (Figure 2D). Each
319 injection created an experimental dyke whose propagation occurred first vertically until it
320 reached the interface of the more rigid, overlying gelatine layer, and then occurred
321 laterally, creating a blade-like dyke. Each experiment allowed the injection of up to 4
322 successive dykes (D_i, where i = 1 to 4). Successive experimental dykes were injected at
323 specific spatial intervals (Table 2) measured horizontally at the base of the tank from
324 one injection point to the next. Each injection point was located along a line through the
325 centre of the base of the tank, parallel to the extension direction. Injections were
326 stopped before they could reach either the surface or the tank walls, and each dyke was
327 allowed to solidify before another was made. These dykes were not expected to
328 coalesce (Takada, 1994b); indeed in most cases, they did not. A few experimental
329 injections (D_i) did merge with a previous injection (D_{i-1}) and flowed along a solidified
330 edge. If this occurred at a late stage, measurements were recorded prior to their
331 coalescence; otherwise these dykes were removed from further analysis. Occasionally

a dyke showed evidence of small beads of gelatine accumulating at the base of the fluid injection. This indicated some melting of the gelatine had occurred and these dykes were also removed from further analysis.

At the end of each experiment, the static spatial relationship, shape and orientation between successive injections were recorded. The spacing between each injection (d_s), the injection temperature, the gelatine temperature, the injection's volumetric flux, the injection time, and the injection orientation (or rotation angle) (γ) are given in Table 2. The rotation angle of each dyke (D_i) was measured relative to the orientation of the previous dyke (D_{i-1}) from an aerial photograph of the dyke's final position (Figure 4 A). The dyke orientation will be dependent on the extensional stress field set up within the gelatine; the stress field will be altered by each subsequent dyke. The injection length and thickness were measured after the experiment ceased by excavating the solidified injections from the gelatine; the thickness was measured at the central point along the length of the dyke where the injection was the thickest.

FIGURE 4 (FIGURE4_ExperimentsDiag9.pdf)

RESULTS AND ANALYSIS

The orientation of the experimental dykes was observed to vary from experiment to experiment. Figure 5 shows the rotation angle between injections as a function of the injection spacing (d_s), with different symbols representing different amounts of imposed extension, and indicates that the rotation angle between two successive experimental dykes (D_i and D_{i+1}) decreases as the separation distance, and/or the extension

undergone by the solid, increase. Some of the experimental dykes (D_{i+1}) were observed to propagate further in lateral extent than the previous dyke (D_i). The average propagation direction of dykes that emerge from the shadow of the previous dyke will be different to those that do not exceed the length of the previous dyke. Where dykes emerge from the shadow of a previous dyke, the propagation direction will alter as the stress field necessarily changes (e.g. Figure 4A). In an extensional environment, the result will be to cause the dyke to realign to propagate perpendicular to the extension direction, as seen in the experiments, whilst dykes remaining in the shadow of the previous dyke will feel the presence of the previous dyke along their entire length. For any dyke (D_{i+n}) that exceeded the lateral extent of the previous dyke and altered its propagation direction, the average strike of the beginning part of the dyke was recorded as that dyke's orientation (e.g. Figure 4A).

Gelatine is deformed the most where a dyke is the thickest, which is usually near its centre. We therefore assume that the thickness at the centre of an experimental dyke is a proxy for the altered stress field that controls the orientation of the subsequent dykes, and that the accumulated dyke thickness from the injection of more than one dyke will affect the shape, orientation and emplacement of the next dyke intruded. In reality, the whole shape of the previous intrusion could be important but we make the simplifying assumption that the thickness of a dyke at its centre has the greatest influence. We also neglect the complicating fact that whether a dyke has a curved or straight shape will alter the existing stress field in a different way.

FIGURE 5 (FIGURE5_SpacingVSangle130215bw.pdf)

The normal and tangential stresses associated with the opening of a single crack in an infinite elastic medium can be calculated, along with the theoretical maximum aperture of a crack, using Hooke's law and the analysis of Westergaard (1939). We consider the case of a 2D crack aligned parallel and normal to the x and y directions, respectively, with an internal overpressure P_I (the difference between the pressure within the crack and the surrounding stress acting normal to the crack wall), and taking compressive stresses as positive. The calculations are based on three complex functions:

$$Z = \frac{P_I}{\sqrt{\left(1 - \frac{h^2}{z^2}\right)}} - P_I \quad , \tag{6}$$

where h is the crack half-length (in our case, the height of the experimental intrusion, the second longest dimension) and *z* is the complex variable $z = x + iy$;

$$Z' = \frac{dZ}{dz} = -P_I \frac{h^2}{\left(z^3 \left(1 - \frac{h^2}{z^2}\right)^{\frac{3}{2}}\right)} \quad ; \tag{7}$$

and

$$\bar{Z} = P_I \sqrt{(z^2 - h^2)} - P_I z, \tag{8}$$

where *Z* is the derivative of $\bar{Z}$

$$Z = \frac{d\bar{Z}}{dz}. \tag{9}$$

The normal (s_x, s_y) and tangential (τ_{xy}) stresses around the crack, that are induced by its opening, are then

$$s_x = Re(Z) - y\,Im(Z') \tag{10}$$

$$s_y = Re(Z) + y\,Im(Z') \tag{11}$$

$$\tau_{xy} = -y\,Re(Z'), \tag{12}$$

and the associated displacements are

$$u_x = \left((1 - 2\nu)\,Re(\bar{\bar{Z}}) - y\,Im(\bar{Z})\right)\frac{(1+\nu)}{E} \tag{13}$$

$$u_y = (2(1-\nu)\,Im(\bar{Z}) - y\,Re(\bar{Z}))\,\frac{(1+\nu)}{E}\,. \tag{14}$$

This analysis enabled us to calculate the internal pressure within our first experimental dykes ($D_{i=1}$) by comparing the measured maximum aperture of these experimental dykes with the theoretical maximum aperture predicted for a range of different overpressures. The internal overpressure (P_I) that gave the minimum mismatch between the measured and theoretical maximum aperture was chosen (Table 2). In doing so, we assumed our experimental dykes could be approximated as 2D objects given their large length to thickness aspect ratios. The first injection overpressure was almost always larger than the applied remote tensile stress (Experiments 16-19 were exceptions), implying that the opening of the first crack $D_{i=1}$ not only accommodated entirely the applied tensile stress but required also some additional overpressure (Table 3). The thickness of each dyke acts to reduce the remote tensile stress and increase the compressional stress within the gelatine, deforming the crust around it. As dykes are progressively intruded into a gelatine block, the gelatine stress state will transition into being locally more compressive. The remote tensile stress applied to Experiments 16-

19 was not overcome by the first dyke, this is presumably because these experiments were the ones with the largest gelatine extension (30 mm) and had the largest initial applied tensile stress.

As shown in Figure 6, the opening of a dyke induces a local compression of the host elastic solid. This causes the subsequent injected dykes to rotate (Figure 6), but it also reduces the thickness of the intrusions.

FIGURE 6 (FIGURE6_Westergaard-BW3.pdf)

The stress perturbation induced by the opening of a dyke varies with space and decreases away from the crack. This perturbation is the greatest near the centre of the crack because its opening is the largest there. We have found an analytical approximation for the compressive component s_y induced by the opening of the crack and acting normal to its long axis, and we used this approximation to analyse its effect on the orientation of the subsequent cracks. The decay of the stress, normalised by the crack internal pressure, away from the centre of the crack at $x = 0$ can be approximated by the function

$$s_y = \frac{1}{(1+\frac{(d_s)^2}{\sqrt{\pi h^2}})} \quad (15)$$

where d_s is the distance from the centre of the crack and h is the crack half-height (the relevant length for a 3D crack in an elastic medium is its second longest dimension, i.e. the crack height for horizontally propagating dykes). The boundary conditions for this equation are identical to those of Westergaard (1939), where a crack is embedded in an infinite elastic medium and is opening under constant internal pressure. This allows a

comparison between the analytical expression and Westergaard's solution to be resolved numerically. Figure 7 A shows the exact spatial evolution of the normal stress (s_y) away from the centre of the crack along the y-axis and normalised by the internal pressure (black line), calculated numerically using Westergaard's (1939) analysis (equation 11), as well as our analytical approximation (equation 15).

FIGURE 7 (FIGURE7_LABwestergaardAnalysisandFigures180714.pdf)

Figure 7 B shows the residual between the exact and approximate solutions and shows that the approximation is correct to within 3.5% of the exact solution or less. Since σs_y will be greatest along the direction x = 0, this analytical function represents an upper bound approximation for the spatial evolution of the compressive stress component $s\sigma_y$ around the crack (Figure 7 A, red line).

This analysis of the stress around an opening crack confirms as expected that the natural length scale of the injections is the injection half-length (the dyke half-height in our experimental configuration). Therefore it is assumed that the rotation angle γ between dyke D_i and D_{i+1} depends only on 1) the stress ratio of the remote tensile stress (σ_y) to the first injection ($D_{i=1}$) overpressure (P_o, the source fluid pressure in excess of the lithostatic pressure prior to imposing a remote tensile stress), and 2) the injection spacing (d_s) between D_i and D_{i+1} normalised by the half-height (h) of D_i which is the relevant length in the experiments:

$$\gamma = f\left(\frac{\sigma_y}{P_o}, \quad \frac{d_s}{h}\right). \tag{16}$$

The effect of both of these ratios should be independent of one another as neither σ_y nor d_s is dependent on the other. Therefore

$$\gamma = f\left(\frac{\sigma_y}{P_o}\right) . g\left(\frac{d_s}{h}\right) \quad (17)$$

where *f* and *g* are unknown functions. For a case of no remote tensile stress (σ_y = 0), γ should reflect the stress perturbation of the opening of the crack D_i. As shown in Figure 7, the stress perturbation (σ_p) due to the crack opening, decreases approximately as

$$\sigma_p = \frac{1}{\left(1 + \frac{(d_s)^2}{(\sqrt{\pi}\, h^2)}\right)} \quad (18)$$

where d_s is the injection spacing, or the distance from the crack centre parallel to the opening. Therefore

$$g\left(\frac{d_s}{h}\right) = \frac{1}{\left(1 + \frac{(d_s)^2}{(\sqrt{\pi}\, h^2)}\right)} . \quad (19)$$

In the case of a fluid overpressure much greater than the remote stress, $P_o >> -\sigma_y$, the rotation angle will likely be maximised and so equal to π/2 radians. In the opposite case, when $-\sigma_y >> P_o$, the stress perturbation induced by the opening of the first crack should be minimal and so the rotation angle should be zero. Considering the stress ratio P_o/σ_y, it is thus expected that the ratio of $\gamma/(\pi/2)$ radians → 1 when $-P_o/\sigma_y >> 1$, and $\gamma/(\pi/2)$ radians → 0 when $-P_o/\sigma_y << 1$. The function $\frac{(-P_o/\sigma_y)}{(-P_o/\sigma_y + 1)}$ behaves in the same way, thus the function *f* is approximated as

$$f = -\frac{\pi}{2}\frac{\left(\frac{P_o}{\sigma_y}\right)}{\left(1 - \frac{P_o}{\sigma_y}\right)} \quad . \tag{20}$$

460 P_o is not known but it is related to the effective crack overpressure (P_I), which is the sum
461 of the fluid overpressure (P_o) and the remote tensile stress (σ_y):

$$P_I = P_o - \sigma_y \quad . \tag{21}$$

462 So the ratio $P_o/\sigma_y = P_I/\sigma_y + 1$, and the function *f* becomes

$$f = \frac{\pi}{2}\left(1 + \frac{\sigma_y}{P_I}\right) \quad . \tag{22}$$

463 We note, however, that the fluid overpressure P_o cannot be negative (it can only be
464 equal to zero at minimum), and so the stress ratio $-P_o/\sigma_y$ is always greater than or equal
465 to 0, which is equivalent to having $-P_I/\sigma_y \geq 1$, that is $-\sigma_y/P_I \leq 1$. Therefore the
466 function *f* should be defined as

$$f\left(-\frac{\sigma_y}{P_I} \leq 1\right) = \frac{\pi}{2}\left(1 + \frac{\sigma_y}{P_I}\right), \tag{25}$$

467 and

$$f\left(-\frac{\sigma_y}{P_I} > 1\right) = 0 \quad . \tag{24}$$

468 Therefore we expect the rotation angle between two successive fluid cracks to be

$$\gamma = \begin{cases} \dfrac{\frac{\pi}{2}\left(1 + \frac{\sigma_y}{P_I}\right)}{1 + \left(\frac{(d_s)^2}{\sqrt{\pi}\,\omega^2}\right)} & \text{when} -\dfrac{\sigma_y}{P_I} \leq 1, \\ 0 & \text{when} -\dfrac{\sigma_y}{P_I} > 1. \end{cases} \quad (25)$$

Figure 8A compares the surface of expected γ values defined by Equation 25 with the measured rotation angles. The majority of the experimental data fall on the expected surface within the experimental error, estimated to be +/- 10 degrees (Figure 8B).

FIGURE 8 (FIGURE8_WestergaardModel01-02-152.pdf)

DISCUSSION

The results confirm as expected that the orientation of the first injection ($D_{i=1}$) occurs perpendicular to the maximum extensional stress, consistent with observations of dyke injections intruding along the rift zone of active segments of spreading rift margins (e.g. Schwarz et al., 2005; Buck et al., 2006; Hamling, 2010). The experiments have shown that for repeated injections into a region, the angle of rotation between an injection and the next is dependent on the ratio of the overpressure of the fluid and the remote tensile stress. For thinner and shorter first injections, where the overpressure due to the fluid is small, the rotation angle between the injection (D_i) and the subsequent one (D_{i+1}) is also small. For large first injections, the rotation angle γ between the injection (D_i) and a subsequent injection (D_{i+1}) is larger. The rotation angle is dependent on the first injection overpressure, and is inversely proportional to the square of the spacing normalised by the crack half-height (Equation 25). This inverse relationship with

487 normalised spacing implies that for larger normalised spacings, the rotation angle will be
488 decreased.

489 The experiments presented here show that, in addition to orientation changes due to
490 regional stresses, the dyke injections themselves can impart sufficient stress onto the
491 host rock they are intruding, that they alter the propagation path of subsequent dykes.
492 This has also been seen by Kavanagh and Sparks (2011) where propagating dykes
493 entering rock layers with different mechanical properties were observed to rotate and
494 create a scissor-like profile. Ito and Martel (2002) studied the convergence and
495 coalescence of fluid-filled fractures due to the alteration of the local stress field by a
496 previous dyke injection. To allow coalescence, they found that the injection spacing had
497 to be less than a few dyke head-lengths and that the applied remote stress is small
498 compared with the driving pressure. In our experiments, the injection spacing was
499 always within the required distance for crack convergence, but we did not observe any
500 coalescence or rotation about a horizontal axis; this is likely to be because the remote
501 stress field is large. Our results are instead consistent with the findings of Ito and Martel
502 (2002), Olson and Pollard (1989) and Takada (1994a), that an increase in the remote
503 tensile stress will reduce the interaction of dykes.

504 In most of our experiments, the imposed regional extensional stress field seems to have
505 been overcome by the first injection. Thus for successive injections, the stress field
506 became progressively more compressive, allowing the injections to rotate to an
507 orientation almost perpendicular to the first injection ($D_{i=1}$) in some cases.The recent
508 activity (Figure 1) taking place on the subaerially exposed Manda Hararo-Dabbahu
509 segment of the Red Sea Rift (e.g. Wright et al., 2006; Daniels et al., 2014) can be

examined using the same relationship as the experiments (Equation 25). Taking the first injection in the recent sequence of dyke injections (Figure 1E), an estimate of the range of expected distances between the successive intrusions, given their emplacement orientation, can be made. This requires the knowledge of a range of plausible rotation angles for the dykes in the sequence, the effective overpressure P_l that caused the opening of the first dyke, and the remote tensile stress σ_y. The stress drop Δs caused by the opening of the initial dyke in the recent intrusion sequence, has been estimated to be 30-80 MPa (Grandin et al., 2010; Hamling et al., 2010). This is a compressive stress induced by the opening of the dyke, over and above the remote tensile stress σ_y acting on the crust at that point. The amount of remote tensile stress σ_y on the Red Sea Rift is not known, however, the tectonic force available for rifting is usually estimated to be in the range of 3-5 Tera N/m (Forsyth and Uyeda, 1975; Solomon et al., 1980; Buck 2004) with 4.2 Tera N/m the standard case (Bialas et al., 2010). Divided over the thickness of the crust at the Red Sea Rift in Afar, Ethiopia, this force provides -120 to -200 MPa of remote tensile stress, with -168 MPa as the standard case. Therefore, P_l can be estimated as $P_l = \Delta s - \sigma_y$, thus in the range of 198 to 248 MPa. These values of P_l and σ_y correspond to an overall range for the ratio $-\sigma_y/P_l$ of 0.68 to 0.85.

The strike directions of the dykes after September 2005 have been estimated to be in the range 327.8 to 343.1 (Hamling et al., 2009; Hamling 2010; Ebinger et al., 2010). This estimate range was obtained using a model of ground deformation derived from INSAR. If we take the difference between the strike of dyke D_i and dyke D_{i+1}, a range of rotation values that represent the effect of a dyke on the subsequent one can be calculated. Successive dykes from the Afar rifting episode produce rotation values in the

range 2.3 to 12.5^{o}. The caveat however is that the dykes are not completely overlapping in all cases. The Afar rifting episode shares many similarities with the Krafla rifting episode (1975-1984) (Figure 1E), however the understanding of the 3D distributions of the dyke openings along the fissure swarm length is less well constrained (Hollingsworth et al., 2012; Hollingsworth et al., 2013). Pollard et al., (1983) use vertical displacements and surface faulting to infer the strike direction of dykes intruded into Kilauea's Southwest rift zone in May 1970, September 1971 and December 1971. The differences in strike direction between these three dykes give rotation angles of 5 and 2^{o} respectively, within the range of those measured in Afar.

Using this range of rotation angles, a range of expected dyke spacings can be calculated. For a rotation of only 1^{o}, the spacing is expected to be in the range 16.5 to 24.6 km, depending on the value used for the ratio $-\sigma_y/P_l$ (Figure 9). A spacing of 16 to 25 km seems unreasonably large; however, these distances correspond to a very small rotation angle. A rotation of 13^{o} corresponds to injection spacings of up to 5.1 km, well within the 10 km wide injection region beneath the rift axis, revealed by various geophysical surveys (e.g. Johnson, 2012). Figure 9 illustrates that to get injections within ~5 km from the rift axis, as observed on the Red Sea Rift in Afar, would result in a minimum rotation of 7-13^{o}.

FIGURE 9 (FIGURE9_EstimatedSpaceandOrientation2.pdf)

The histogram of the simulated injection spacing frequency (Figure 9B) provides an idea of the most likely injection spacing values that would be expected on the Red Sea Rift for the range of observed Θ and calculated stress ratio $-\sigma_y/P_l$. It shows that the most

555 frequently occurring injection spacing is 4000 to 5000 m (15.3% of the data), and that
556 nearly half of the data (48%) are ≤6 km spacing. For the range of stress ratios and
557 rotation angles observed on the Red Sea Rift, the majority of the dykes are predicted to
558 intrude within 10 km of the previous one and most frequently between 4 and 5 km,
559 which is consistent with the results of previous geophysical surveys of the area (e.g.
560 Johnson, 2012).

561 Extensional stresses at plate margins are relieved by dyke injections events; between
562 injections, extensional stresses are able to build up. The tendency for repeated dyke
563 injection events to eventually relieve all of the extensional stresses existing in the host
564 rocks they are intruding is likely to be a strong function of the time between injection
565 events. An estimate of the stress build-up rate at a rifted plate margin can be made from
566 the product of the host-rock Young's modulus and the strain rate (e.g. Timoshenko and
567 Goodier, 1970). For a typical Young's modulus of 10 GPa and a tectonic strain rate of
568 10^{-14} s^{-1}, a stress build-up rate of 3 kPa yr^{-1} would be expected. The remote tensile
569 stress available for rifting on the Red Sea Rift is calculated to be -120 to -200 MPa. The
570 stress build-up rate suggests that this remote tensile stress would have taken between
571 40 and 67 ka to accrue. This timescale would be even longer if the crust started in a
572 state of compressional stress (i.e. after a period of protracted dyke injection). Dyke
573 injections with overpressures on the order of 100 MPa would overcome the remote
574 tensile stress after just a couple of injections. After a larger dyke injection, the time
575 taken for the extensional stress to reach the same level as that prior to the injection will
576 be longer.

Stress relaxation on the other hand will tend to reduce, through time, the local compressional stress exerted on the surrounding crust by a dyke injection. The amount of stress relaxation will depend on the thermal state of the crust following the injections, as hotter crust will relax more quickly, as well as the time between successive injections, because higher injection frequency will both reduce the amount of stress relaxation that can occur and lead to increase local, intrusion-induced, compressional stress. Provided that the stress build-up is slow and that the timescale between repeated injections is smaller than the stress relaxation timescale, individual dyke injections within multi-injection episodes should start to experience rotation after only a few injections. Rotation of the orientation of dyke injections about their vertical axis at active rift margins has been documented at transform faults (e.g. MacLeod et al., 1990); dyke injections at rift margins mostly seem to occupy orientations that are approximately rift-parallel. This suggests that the extensional stress at rift margins is larger than the amount that is relieved by dyke injections, or that the elapsed time between dyke intrusions is longer than the time taken for extensional stresses to build up in the crust.

CONCLUSIONS

The experiments conducted in this study investigate the effect of multiple dyke injections under extensional tectonic stresses. Based on these experiments, we find a relationship between the amount of rotation (or the emplacement orientation) of successive dykes intruded at a given distance from each other and under given extensional stress conditions.

599 The experimental results show that the orientation of the first injection occurs
600 perpendicular to the maximum extensional stress and that the size of the first injection is
601 important as it determines how much of the extensional stress is locally relieved. The
602 angle of rotation between the first injection and the next depends on the ratio of the fluid
603 overpressure and the remote tensile stress. For small first injections, where the fluid
604 overpressure is small, the rotation angle between the injection and the subsequent one
605 is also small. For large first injections, the rotation angle between the injection and a
606 subsequent injection is larger. More specifically, the rotation angle is dependent on the
607 first injection overpressure and is inversely proportional to the square of the normalised
608 spacing with respect to the height of the first injection (Equation 25), so that a larger
609 normalised spacing will lead to a smaller rotation angle between successive intrusions.
610 Conversely, the knowledge of rotation angles between successive intrusions within rift
611 zones allows for an estimation of the spatial distribution of these intrusions. For the
612 range of stress ratios and rotation angles observed on the actively spreading Red Sea
613 rift, the vast majority of the dykes are predicted to intrude within 10 km of the previous
614 one and most frequently between 4 and 5 km. This is consistent with geophysical
615 observations of dyke locations on the Red Sea Rift in Afar, Ethiopia.

616

617 **ACKNOWLEDGEMENTS**

618 The majority of the data for this paper are presented in Tables 1 to 3. Some additional
619 data are available in the author's PhD thesis (Modelling magma transport: a study of

dyke injection, 2013) accessible through the University of Bristol library, or online at the British Library EThOS service.

KAD would like to thank C. Clapham for building the experimental apparatus and J. L. Kavanagh and F. Witham for assistance in the laboratory. Discussions with, and constructive comments on an earlier version of this manuscript by J. L. Kavanagh and R. S. J. Sparks have been instrumental in improving this work. G. A. Jones is also thanked for helpful comments and suggestions. KAD was supported by a NERC Consortium Grant. This research was partially funded by the French Government Laboratory of Excellence initiative ANR-10-LABX-0006, the Région Auvergne, and the European Regional Development Fund. This is Laboratory of Excellence ClerVolc contribution number 137.

REFERENCES

Allerton, S., 1989. Fault block rotations in ophiolites: results of palaeomagnetic studies in the Troodos Complex, Cyprus. In Palaeomagnetic Rotations and Continental Deformation (Kissel, C., and Laj, C., Editors). Vol. 254. NATO ARI Series C.

Allerton, S., Vine, F. J., 1991. Spreading evolution of the Troodos ophiolite, Cyprus: Some palaeomagnetic constraints. Geology 15, 593 – 597.

Bastow, I. D., Keir, D., 2011. The protracted development of the continent-ocean transition in Afar. Nature Geoscience 4, 248 – 250.

640 Bialas, R. W., Buck, W. R., Qin, R., 2010. How much magma is required to rift a
641 continent? Earth and Planetary Science Letters 292, 68 – 78.

642 Bonhommet, N., Roperch, P., Calza, F., 1988. Palaeomagnetic arguments for block
643 rotations along the Arakapas fault (Cyprus). Geology 16, 422 – 425.

644 Buck, W. R., 2004. Consequences of asthenospheric variability on continental rifting. In
645 Rheology and Deformation of the Lithosphere at Continental Margins (Karner, G. D., et
646 al., Editors). Columbia University Press.

647 Buck, W. R., 2006. On the frequency of dike intrusion episodes at spreading centers.
648 Eos Transactions, AGU 87 (52) Fall Meeting Supplement, Abstract T41B-1566.

649 Buck, W.R., Einarsson, P., and Brandsdottir, B., 2006. Tectonic stress and magma
650 chamber size as controls on dike propagation: Constraints from the 1975–1984 Krafla
651 rifting episode. Journal of Geophysical Research 111 (B12404),
652 doi:10.1029/2005JB003879.

653 Chanceaux and Menand, 2014. Solidification effects on sill formation: an experimental
654 approach. Earth and Planetary Science Letters 403, 79 – 88.

655 Crisp, J., 1952. The Use of Gelatin Models in Structural Analysis. Proceeding IB of the
656 Institute of Mechanical Engineers 12, 580 – 604.

657 Dahm, T., 2000a. Numerical simulations of the propagation path and the arrest of fluid-
658 filled fractures in the earth. Geophysical Journal International 141, 623 – 638.

659 Dahm, T., 2000b. On the shape and velocity of fluid-filled fractures in the Earth.
660 Geophysical Journal International 142, 181 – 192.

661 Daniels, K. A., Kavanagh, J. L., Menand, T., Sparks, R. S. J., 2012. The shapes of
662 dykes; evidence for the influence of cooling and inelastic deformation. Bulletin of the
663 Geological Society of America 124 (7-8), 1102 – 1112.

664 Daniels, K.A., Bastow, I.D., Keir, D., Sparks, R.S.J. and Menand, T., 2014. Thermal
665 models of dyke intrusion during development of continent–ocean transition. Earth and
666 Planetary Science Letters 385, 145-153.

667 Delaney, P. T., Pollard, D. D., 1982. Solidification of basaltic magma during flow in a
668 dyke. American Journal of Science 282, 856 – 885.

669 Dietrich, D., Spencer, S., 1993. Spreading-induced faulting and fracturing of oceanic
670 crust: examples from the Sheeted Dyke Complex of the Troodos ophiolite, Cyprus. In
671 Magmatic Processes and Plate Tectonics (Pritchard, H. M., Alabaster, T., Harris, N. B.
672 W., and Neary, C. R., Editors). Geological Society Special Publication No. 76, 121 –
673 139.

674 Dilek, Y., Thy, P., Moores, E. M., Ramsden, T. W., 1990. Tectonic evolution of the
675 Troodos opiolite within the Tethyan framework. Tectonophysics 9, 811 – 823.

676 Ebinger, C. J., Ayele, A., Keir, D., Rowland, J., Yirgu, G., Wright, T., Belachew, M.,
677 Hamling, I., 2010. Length and Timescales of Rift Faulting and Magma Intrusion: The
678 Afar Rifting Cycle from 2005 to Present. Journal of Geophysical Research 38, 437 –
679 464.

680 Einarsson, P., 1991. The Krafla rifting episode 1975 - 1989, in Náttúra Mývatns (The
681 Nature of Lake Mývatn), pp. 97 – 139, Icelandic Nature Sci. Soc., Reykjavík.

682 Farquharson, F., Hennes, R., 1940. Gelatin models for photoelastic analysis of stress in
683 earth masses. Civil Engineering 10 (4), 211 – 214.

684 Fiske, R. S., Jackson, E. D., 1972. Orientation and Growth of Hawaiian Volcanic Rifts:
685 The Effect of Regional Structure and Gravitational Stresses. Proceedings of the Royal
686 Society of London A 329 (1578), 299 – 326.

687 Forsyth, D. W., Uyeda, S., 1975. On the relative importance of driving forces of plate
688 motion. Geophysical Journal of the Royal Astronomical Society 43, 163 – 200.

689 Fridleifsson, I. B., 1977. Distribution of large basaltic intrusions in the Icelandic crust and
690 the nature of the layer2/layer3 boundary. Bulletin of the Geological Society of America
691 88, 1689 – 1693.

692 Galerne, C. Y., Galland, O., Neumann, E.-R., Planke, S., 2011. 3D relationships
693 between sills and their feeders: Evidence from the Golden Valley Sill Complex (Karoo
694 Basin) and experimental modelling, Journal of Volcanology and Geothermal Research,
695 202, 189 – 199.

696 Galland, O., d'Ars, J. D. B., Cobbold, P. R., Hallot, E., 2003. Physical models of
697 magmatic intrusion during thrusting. Terra Nova 15 (6), 405 – 409.

698 Galland, O., Cobbold, P. R., Hallot, E., d'Ars, J. D. B., Delavaud, G., 2006. Use of
699 vegetable oil and silica powder for scale modelling of magmatic intrusion in a deforming
700 brittle crust. Earth and Planetary Science Letters 243, 786 – 804.

701 Galland, O., Cobbold, P. R., d'Ars, J. D. B., Hallot, E., 2007. Rise and emplacement of
702 magma during horizontal shortening of the brittle crust: Insights from experimental
703 modelling. Journal of Geophysical Research 112 (B6), B06402.

704 Galland, O., Cobbold, P. R., Hallot, E., d'Ars, J. D. B., 2008. Magma-controlled tectonics
705 in compressional settings: insights from geological examples and experimental
706 modelling. Bollettino Della Societa Geologica Italiana 127 (2), 205 – 208.

707 Galland, O., Planke, S., Neumann, E. R., Malthe-Sorenssen, A., 2009. Experimental
708 modelling of shallow magma emplacement: Application to saucer-shaped intrusions.
709 Earth and Planetary Science Letters 277 (3 - 4), 373 – 383.

710 Grandin, R., Socquet, A., Jacques, E., Mazzoni, N., deChabalier, J.-B., King, G. C. P.,
711 2010. Sequence of rifting in Afar, Manda-Hararo rift, Ethiopia, 2005-2009: Time-space
712 evolution and interactions between dikes from interferometric synthetic aperture radar
713 and static stress change modeling. Journal of Geophysical Research 115 (B10413), 18.

714 Gudmundsson, A., 2006. How local stresses control magma-chamber ruptures, dyke
715 injections, and eruptions in composite volcanoes. Earth Science Reviews 79, 1 – 31.

716 Gudmundsson, A., and Brenner, S. L., 2001. How hydrofractures become arrested.
717 Terra Nova 13 (6), 456 - 462.

718 Hamling, I. J., 2010. Measuring and modelling deformation during the Dabbahu (Afar)
719 rifting episode. Ph.D. thesis, University of Leeds.

720 Hamling, I. J., Ayele, A., Bennati, L., Calais, E., Ebinger, C. J., Keir, D., Lewi, E., Wright,
721 T. J., Yirgu, G., 2009. Geodetic observations of the ongoing Dabbahu rifting episode:

new dykes intrusions in 2006 and 2007. Geophysical Journal International 178 (2), 989 – 1003.

Hamling, I. J., Wright, T. J., Calais, E., Bennati, L., Lewi, E., 2010. Stress transfer between thirteen successive dyke intrusions in Ethiopia. Nature Geoscience 3, 713 – 717.

Heimpel, M., Olson, P., 1994. Buoyancy-driven fracture and magma transport through the lithosphere: models and experiments. In Magmatic Systems (Ryan, M. P., Editor). Academic Press, Inc, 223 – 240.

Hollingsworth, J., Leprince, S., Ayoub, F., Avouac, J.-P., 2012. Deformation during the 1975 – 1984 Krafla rifting crisis, NE Iceland, measured from historical optical imagery. Journal of Geophysical Research 117 (B11407), doi:10.1029/2012JB009140,

Hollingsworth, J., Leprince, S., Ayoub, F., Avouac, J.-P., 2013. New constraints on dike injection and fault slip during the 1975–1984 Krafla rift crisis, NE Iceland. Journal of Geophysical Research 118 (3707–3727), doi:10.1002/jgrb.50223.Holness, M. B., and Humphreys, M. C. S., 2003. The Traigh Bhan na Sgurra Sill, Isle of Mull: Flow Localization in a Major Magma Conduit. Journal of Petrology 44 (11),1961 – 1976.k

Hyndman, D., Alt, D., 1987. Radial dikes, laccoliths, and gelatin models. Journal of Geology 95, 763–774.

Ito, G., Martel, S. J., 2002. Focusing of magma in the upper mantle through dike interaction. Journal of Geophysical Research 107 (B10), 16 – 17.

742 Johnson, N., 2012. Continental rifting to sea-floor spreading: Collection, analysis and
743 visualisation of magnetotelluric data from Afar. Ph.D. thesis, University of Edinburgh.

744 Johnson, A., Pollard, D. D., 1973. Mechanics of growth of some laccolithic intrusions in
745 the Henry Mountains, Utah: I. Field observations, Gilberts model, physical properties
746 and flow of the magma. Tectonophysics 18, 261 – 309.

747 Kavanagh, J., Menand, T., Sparks, R. S. J., 2006. An experimental investigation of sill
748 formation and propagation in layered elastic media. Earth and Planetary Science Letters
749 245, 799 – 813.

750 Kavanagh, J. L., and Sparks, R. S. J., 2011. Insights of dyke emplacement mechanics
751 from detailed 3D dyke thickness datasets. Journal of the Geological Society 168 (4),
752 965 – 978.

753 Kavanagh, J., Menand, T., Daniels, K. A., 2013. Gelatine as a crustal analogue:
754 Determining elastic properties for modelling magmatic intrusions. Tectonophysics 582,
755 101-111.

756 Kavanagh, J. L., and Pavier, M. J, 2014. Rock interface strength influences fluid-filled
757 fracture propagation pathways in the crust. Journal of Structural Geology 63, 68 – 75.

758 Keir, D., Hamling, I. J., Ayele, A., Calais, E., Ebinger, C., Wright, T. J., Jacques, E.,
759 Mohammed, K., Hammond, J. O. S., Belachew, M., Baker, E., Rowland, J. V., Lewi, E.,
760 Bennati, L., 2009. Evidence for focussed magmatic accretion at segment centres from
761 lateral dike injections captured beneath the Red Sea Rift in Afar. Geology 37 (1), 59 –
762 62.

763 Kervyn, M., G. G. J. Ernst, van Wyk de Vries, B., Mathieu, L., and Jacobs, P., 2009.
764 Volcano load control on dyke propagation and vent distribution: Insights from analogue
765 modelling. Journal of Geophysical Research 114, B03401, doi:10.1029/2008JB005653.

766 Kühn, D., Dahm, T., 2004. Simulation of magma ascent by dykes in the mantle beneath
767 mid-ocean ridges. Journal of. Geodynamics. 147–159.

768 Kühn, D., Dahm, T., 2008. Numerical modelling of dyke interaction and its influence on
769 oceanic crust formation. Tectonophysics 447, 53-65.g

770 Le Corvec, N., Menand, T., and Lindsay, J., 2013. Interaction of ascending magma with
771 pre-existing crustal fractures in monogenetic basaltic volcanism: an experimental
772 approach. Journal of Geophysical Research 118, 968 – 984.

773 Lin, J., Purdy, G.M., Schouten, H., Sempéré, J.-C., and Zervas, C., 1990, Evidence
774 from gravity data for focused magmatic accretion along the Mid-Atlantic Ridge: Nature,
775 v. 344, p. 627–632.

776 Lister, J. R., Kerr, R. C., 1991. Steady solutions for feeder dykes in a density-stratified
777 lithosphere. Journal of Geophysical Research 96, 10049 – 10077.

778 Maaloe, S., 1987. The generation and shape of feeder dykes from mantle sources.
779 Contributions to Mineralogy and Petrology 96, 47 – 55.

780 MacLeod, C. J., Allerton, S., Gass, L. G., Xenophontos, C., 1990. Structure of a fossil
781 ridge-transform intersection in the Troodos ophiolite. Nature 348, 717 – 720.

782 Maguire, P. K. H., Keller, G. R., Klemperer, S. L., Mackenzie, G. D., Keranen, K.,
783 Harder, S., O'Reilly, B., Thybo, H., Asfaw, L., Khan, M. A., Amha, M., 2006. Crustal

784 structure of the northern Main Ethiopian Rift from the EAGLE controlled source survey;
785 a snapshot of incipient lithospheric break-up. In The Afar Volcanic Province within the
786 East African Rift System (Yirgu, G., Ebinger, C. J., Maguire, P. K. H., Editors). The
787 Geological Society of London, Special Publication no.259.

788 Mathieu, L., Van Wyk de Vries, B., Holohan, E.P., Troll, V.R., 2008. Dykes, cups,
789 saucers and sills: analogue experiments on magma intrusion into brittle rocks. Earth
790 and Planetary Science Letters 271, 1–13.

791 Menand, T., 2008. The mechanics and dynamics of sills in layered elastic rocks and
792 their implications for the growth of laccoliths and other igneous complexes. Earth and
793 Planetary Science Letters 267, 93 – 99.

794 Menand, T., Daniels, K. A., Benghiat, P., 2010. Dyke propagation and sill formation in a
795 compressive tectonic environment. Journal of Geophysical Research 115 (B08201), 1 –
796 12.

797 Menand, T., Tait, S. R., 2001. A phenomenological model for precursor volcanic
798 eruptions. Nature 411, 678 – 680.

799 Menand, T., Tait, S. R., 2002. The propagation of a buoyant liquid-filled fissure from a
800 source under constant pressure: an experimental approach. Journal of Geophysical
801 Research 107 (B11) (2306), 1 – 14.

802 Moores, E. M., Varga, R. J., Verosub, K. L., Ramsden, T., 1990. Regional structure of
803 the Troodos dyke complex. In Ophiolites: Oceanic Crustal Analogues (Malpas, J.,

804 Moores, E. M., Panayiotou, A., and Xenophontos, C., Editors). Geological Survey
805 Department, Nicosia, Cyprus, 27 – 35.

806 Murton, B. J., 1986. Anomalous oceanic lithosphere formed in a leaky transform fault.
807 Evidence from the Western Limassol Forest Complex, Cyprus 143, 845 – 854.

808 Paquet, F., Dauteuil, O., Hallot, E., Moreau, F., 2007. Tectonics and magma dynamics
809 coupling in a dyke swarm of Iceland. Journal of Structural Geology 29, 1477 – 1493.

810 Pollard, D. D., Johnson, A. M., 1973. Mechanics of growth of some laccolithic intrusions
811 in the Henry Mountains, Utah: II. Bending and failure of overburden layers and sill
812 formation. Tectonophysics 18, 311 – 354.

813 Pollard, D. D., Delaney, P. T., Duffield, W. A., Endo, E. T., Okamura, A. T., 1983.
814 Surface deformation in volcanic rift zones. Tectonophysics 94, 541 – 584.

815 Reches, Z., Fink, J., 1988. The mechanism of intrusion of the Inyo Dyke, Long Valley
816 Caldera, California. Journal of Geophysical Research 93 (B5), 4321 – 4334.

817 Richards, R., Mark, R., 1966. Gelatin models for photoelastic analysis of gravity
818 structures. Experimental Mechanics 6 (1), 30 – 38.

819 Righetti, R., Ophir, J., Srinivasan, S., Krouskop, T., 2004. The feasibility of using
820 elastography for imaging the Poisson's ratio in porous media. Ultrasound in Medicine
821 and Biology 30 (2), 215 – 228.

822 Rivalta, E., Bottinger, M., Dahm, T., 2005. Buoyancy-driven fracture ascent:
823 Experiments in layered gelatine. Journal of Volcanology and Geothermal Research 144,
824 273 – 285.

825 Rubin, A. M., 1995. Propagation of magma-filled cracks. Annual Review of Earth and
826 Planetary Sciences 23, 287 – 336.

827 Rubin, A. M., Pollard, D. D., 1987. Origins of blade-like dykes in volcanic rift zones. In
828 Volcanism in Hawai'i . USGS professional paper 1350 (53), 1449 – 1470.

829 Ryan, M. P., 1987. Neutral Buoyancy and the Mechanical Evolution of Magmatic
830 Systems. In Magmatic Processes: Physiochemical Principles (Mysen, B. O., Editor).
831 Special Publication No. 1 of The Geochemical Society.

832 Schwarz, S., Klugel, A., van den Bogaard, P., Geldmacher, J., 2005. Internal structure
833 and evolution of a volcanic rift system in the eastern North Atlantic: the Desertas rift
834 zone, Madeira archipelago. Journal of Volcanology and Geothermal Research 141, 123
835 – 155.

836 Solomon, S. C., Richardson, R. M., Bergman, E. A., 1980. Tectonic stress: models and
837 magnitudes. Journal of Geophysical Research 85, 6086 – 6092.

838 Taisne, B., Jaupart, C., 2009. Dyke propagation through layered rocks. Journal of
839 Geophysical Research 114 (B09203), 18.

840 Taisne, B., Tait, S., 2009. Eruption versus intrusion? Arrest of propagation of constant
841 volume, buoyant, liquid-filled cracks in an elastic, brittle host. Journal of Geophysical
842 Research 114 (B06202), doi:10.1029/2009JB006297.

843 Taisne, B., Tait, S., 2011. Effect of solidification on a propagating dyke. Journal of
844 Geophysical Research 116 (B01206), doi:10.1029/2009JB007058.

845 Takada, A., 1990. Experimental Study on Propagation of Liquid-Filled Crack in Gelatin:
846 Shape and Velocity in Hydrostatic Stress Condition. Journal of Geophysical Research
847 95 (B6), 8471 – 8481.

848 Takada, A., 1994a. Accumulation of magma in space and time by crack interaction. In
849 Magmatic Systems, (Ryan, M. P., Editor). Academic Press Inc, 223 – 240.

850 Takada, A., 1994b. Development of a subvolcanic structure by the interaction of liquid-
851 filled cracks. Journal of Volcanology and Geothermal Research 62, 207 – 224.

852 Thybo, H., Nielsen, C.A., 2009. Magma compensated crustal thinning in continental rift
853 zones. Nature 457, doi:10.1038/nature07688, 873-876.

854 Timoshenko, S. P., Goodier, J. N., 1970. Theory of Elasticity (3rd Edition). McGraw-Hill
855 International, 567 pp.

856 Varga, R. J., Moores, E. M., 1985. Spreading structure of the Troodos ophiolite, Cyprus.
857 Geology 13, 846 – 850.

858 Wadge, G., 1986. The dykes and structural setting of the volcanic front in the Lesser
859 Antilles island arc. Bulletin of Volcanology 48, 349-372.

860 Walter, T. R., and Troll, V. R., 2003. Experiments on rift zone evolution in unstable
861 volcanic edifices. Journal of Volcanology and Geothermal Research 127, 107-120.

862 Watanabe, T., Masuyama, T., Nagaoka, K., Tahara, T., 2002. Analog experiments on
863 magma-filled cracks: Competition between external stresses and internal pressure.
864 Earth Planets Space 54, 1247 – 1261.

865 Westergaard, H. M., 1939. Bearing pressures and cracks. Journal of Applied Mechanics
866 6, A49 – A53.

867 White, R.S., Smith, L.K., Roberts, A.W., Christie, P.A.F., Kusznir, N.J., the rest of the
868 iSIMM Team, 2008. Lower crustal intrusion on the North Atlantic continental margin.
869 Nature 452, doi:10.1038/nature06687, 460-464.

870 Whitehead, J., Dick, J.H.B., and Schouten, H., 1984. A mechanism for magmatic
871 accretion under spreading centres: Nature, v. 312, p. 146–148, doi: 10.1038/312146a0.

872 Wright, T. J., Ebinger, C., Biggs, J., Ayele, A., Yirgu, G., Keir, D., Stork, A., 2006.
873 Magma-maintained rift segmentation at continental rupture in the 2005 Afar dyking
874 episode. Nature 442, 291 – 294.

875

876 **FIGURE CAPTIONS**

877 Figure 1: A and B) The location of the Afar volcanic province within Africa C) The
878 Manda Hararo-Dabbahu rift segment of the subaerial Red Sea Rift (background image
879 courtesy of Prof. K. Whaler). Yellow filled circles denote a volcanic complex, the red
880 lines show the location of the recent dyke activity and the blue arrow shows the
881 direction of extension. The purple line shows the location of the photograph of the fault
882 scarps and normal extension in D). E) The Afar rift dyke swarm (light blue) showing the
883 locations and sizes of the sequential dyke injections between 2005-2009, compared
884 against the dykes injected during the Krafla rifting episode (1975-1984) (black bars).

885 The yellow and red bars denote eruptions. (After Einarsson (1991); Hamling et al.,
886 (2009); Hamling (2010)).

887 Figure 2: A) The experimental apparatus and setup. B and C) The procedure for
888 separating the sides of the gelatine from the walls of the tank. B) Metal plates on two
889 opposing sides of the gelatine were heated with hot water (red shading) and then
890 removed from the tank (red arrows).C) The space vacated by the metal plates was filled
891 with water (blue shading). The remaining sides of the gelatine were cut with a narrow U-
892 shaped metal implement in the direction shown by the green arrows.

893 Figure 3: The value of dimensionless flux and dimensionless temperature for each of
894 the experimental injections from each of the experiments. The different contours
895 correspond to different alpha values. The stars correspond to individual experimental
896 dyke injections. A threshold value of α = 0.5 was set to ensure that a solidification-
897 induced geometry did not occur and only injections with an alpha value below this
898 threshold were used.

899 Figure 4: Example experiments showing the geometry of the experimental set-up and
900 results. A and B) Experiment 26 in plan-view and side-view respectively. C and D)
901 Experiment 38 in plan-view and side-view respectively. The extension direction is
902 shown by the black arrows. The dyke orientation was measured relative to the axis of
903 extension in plan-view (e.g. A and C).

904 Figure 5: Rotation angle as a function of the injection spacing (d_s), colour-coded for
905 different amounts of imposed extension.

Figure 6: Contours (continuous curves) of the normal compressive stress (s_y), calculated using Equation (11), and directions of the maximum compressive principal stress (s_1), both induced by the opening of the crack located between x = -1 and x = 1 (thick black segment). The stresses are normalised by the internal crack overpressure, and the spatial distances are normalised by the crack half-height.

Figure 7: Above: The normal stresses and displacement of the solid due to crack opening. Below: The calculated normal stress due to the opening of a crack (here shown for Experiment 40). A) The exact spatial evolution of the normal stress (s_y) normalised by the internal pressure (P_l) as a function of the distance (d_s) normalised by the crack half-height (h) (black line), and the approximation $1 \,/\, (1 + \frac{(d_s)^2}{\sqrt{\pi\, h^2}})$ (red line). B) The residual between the two solutions.

Figure 8: A) Surface of expected values of rotation angle (γ) as a function of normalised remote tensile stress (σ_y/P_l) and normalised injection spacing (d_s/h). The red dots are the experimental injections. B) The difference between the measured rotation angles and the predicted values from Equation 25. The dashed lines show the experimental error (estimated to be +/- 10 degrees). The vast majority of the measurements fall on the expected surface within experimental error.

Figure 9: A) The rotation angle (γ) against the stress ratio ($-\sigma_y/P_l$), showing the resultant injection spacing (d_s) in km (contours). B) Histogram of the simulated injection spacing (d_s) frequency generated from 1000 randomly generated values for rotation angle (γ) and stress ratio ($-\sigma_y/P_l$), using estimated parameters for the Manda-Harraro Dabbahu rift segment in Afar (see text).

928

929 **TABLE CAPTIONS**

930 Table 1: The gelatine preparation details and experimental starting conditions.

931 Table 2: The experimental injection details and results.

932 Table 3: The experimental dyke measurements.

933

934 **APPENDIX**

935 **Applying an extension to the gelatine**

936 A stationary and unperturbed homogenous block of gelatine has three principle stress
937 directions (σ_x, σ_y and σ_z) acting perpendicular to one another. Initially, there is no
938 horizontal strain, such that

$$\varepsilon_x = \varepsilon_y = 0 \tag{26}$$

939 where ε_x and ε_y are the strains in the *x* and *y* directions, respectively. Because the
940 gelatine's Poisson's ratio is equal to 0.5, this means the initial stress conditions of the
941 block of gelatine are hydrostatic:

$$\sigma_x = \sigma_y = \sigma_z \tag{27}$$

942 where σ_x, σ_y and σ_z are the stresses in the *x*, *y* and *z* directions. Here, compressive
943 stress and strain are taken as positive values. To study a setting where the analogue
944 crust is in extension, the gelatine is compressed in the *z* direction, resulting in an

extension in the *x* direction because the *y* direction is prevented from moving by the sides of the tank. The gelatine extends in the *x* direction according to Hooke's Law, which describes the linear relationship between the stress and strain components (Timoshenko and Goodier, 1970). Hooke's Law relates stress and strain in an elastic solid

$$\varepsilon_x = \frac{1}{E}\left[\sigma_x - \nu\left(\sigma_y y + \sigma_z\right)\right], \tag{28}$$

$$\varepsilon_y = \frac{1}{E}\left[\sigma_y - \nu\left(\sigma_x + \sigma_z\right)\right], \tag{29}$$

$$\varepsilon_z = \frac{1}{E}\left[\sigma_z - \nu\left(\sigma_x + \sigma_y\right)\right], \tag{30}$$

where *E* is the Young's modulus and ν is the Poisson's ratio. The amount of extension is a constant for a particular material. Compression in the vertical *z* direction causes a displacement ΔL and a strain ΔL/L, where L is the original length of the gelatine block in the σ_x direction and ΔL is the horizontal displacement of the gelatine block in the σ_x direction after the imposed stress (see Menand et al. (2010) for further details). $\varepsilon_y = 0$ because movement in this direction is confined by the walls of the tank. For a lot of materials the Poisson's ratio is around 0.25, but because the Poisson's ratio of the gelatine is 0.5 (incompressible) and $\varepsilon_y = 0$, this leads to

$$\varepsilon_z = -\varepsilon_x \ . \tag{31}$$

Therefore Equations (28) to (30) become

$$E\varepsilon_x = \sigma_x - \nu\,\sigma_y - \nu\,\sigma_z\,, \tag{32}$$

$$\sigma_y = \nu\,\sigma_x + \nu\,\sigma_z\ , \tag{33}$$

$$E\varepsilon_z = \sigma_z - \nu\,\sigma_x - \nu\,\sigma_y\ , \tag{34}$$

959 from which we get

$$\sigma_z = \frac{E}{(1-\nu^2)}\,\varepsilon_z + \frac{\nu}{(1-\nu)}\sigma_x\ , \qquad \sigma_y = \frac{\nu E}{(1-\nu^2)}\,\varepsilon_z + \frac{\nu}{(1-\nu)}\sigma_x. \tag{35}$$

960 Because the Poisson's ratio of the gelatine is 0.5, these equations reduce to

$$\sigma_z = \frac{4}{3}E\,\varepsilon_z + \sigma_x \qquad \sigma_y = \frac{2}{3}E\,\varepsilon_z + \sigma_x\ . \tag{36}$$

961 Using numerical calculations conducted computationally with the COMSOL multiphysics
962 package, Menand et al. (2010) showed that in this stress configuration $\sigma_x = 0$, hence

$$\sigma_x = 0\ , \qquad \sigma_y = \frac{2\,E\,\Delta L}{3\,L}\ , \qquad \sigma_z = \frac{4\,E\,\Delta L}{3\,L}\ . \tag{37}$$

963 Using the principle of stress superposition, we can add a uniform stress σ_U without
964 altering the deviatoric stress field (37) so that

$$\sigma_x = 0 + \sigma_U\ , \qquad \sigma_y = \frac{2\,E\,\Delta L}{3\,L} + \sigma_U\ , \qquad \sigma_z = \frac{4\,E\,\Delta L}{3\,L} + \sigma_U\ , \tag{38}$$

965 which is true for any value of σ_U. Choosing

$$\sigma_U = -\frac{4}{3}E\,\varepsilon_z\ , \tag{39}$$

966 and recalling that ε_x = - ε_z = - ΔL/L is negative, we obtain the following deviatoric stress
967 field:

$$\sigma_x = -\frac{4}{3}E\,\frac{\Delta L}{L} \tag{40}$$

$$\sigma_y = -\frac{2}{3}E\,\frac{\Delta L}{L} \tag{41}$$

$$\sigma_z = 0 \tag{42}$$

This is the horizontal tensile stress field created by imposing the vertical compressive strain ΔL/L in the experiments. The amount of vertical compressive stress required to achieve the appropriate amount of horizontal extension was different for each experiment depending on the Young's modulus of the gelatine.

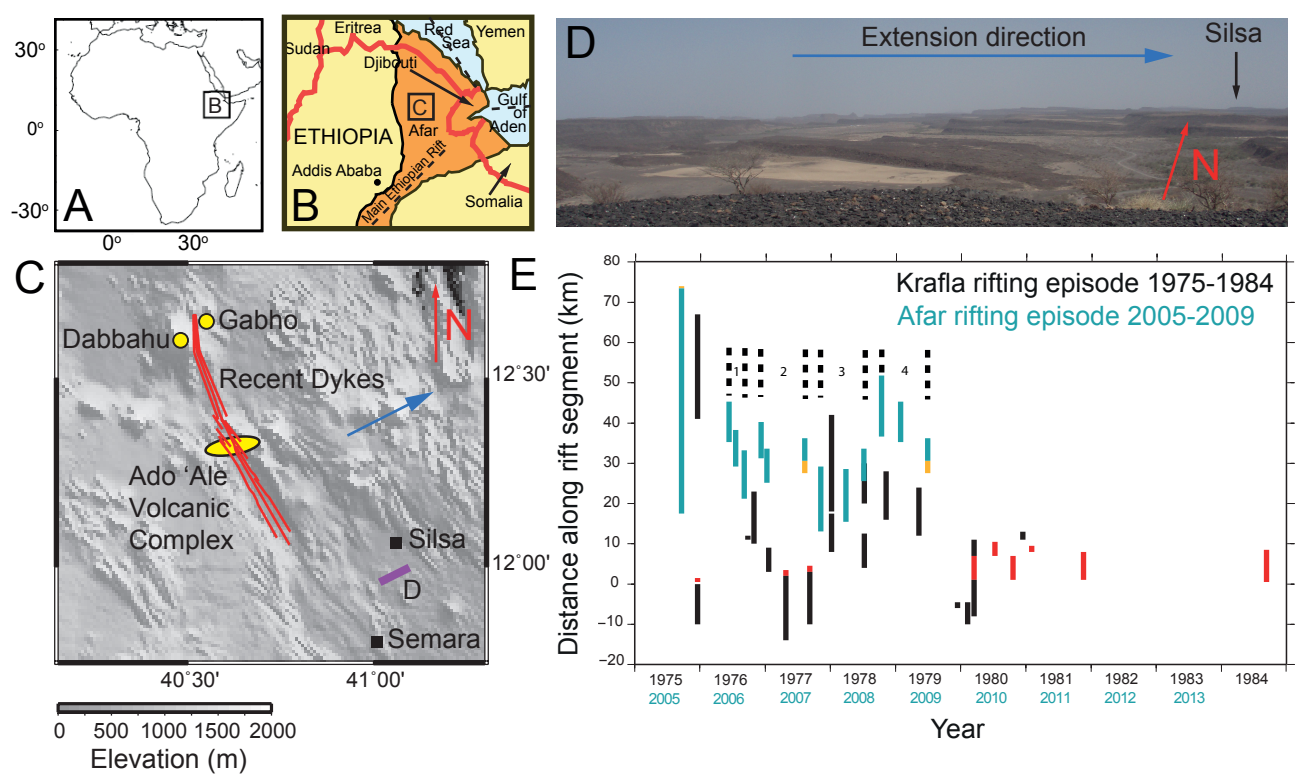
A
30°
0°
-30°
0°
30°
B
B
Eritrea
Red Sea
Yemen
Sudan
Djibouti
C
Gulf of Aden
ETHIOPIA
Afar
Addis Ababa
Main Ethiopian Rift
Somalia
D
Extension direction
Silsa
N
C
Dabbahu
Gabho
N
Recent Dykes
12°30'
Ado 'Ale Volcanic Complex
Silsa
D
12°00'
Semara
40°30'
41°00'
0 500 1000 1500 2000
Elevation (m)
E
Krafla rifting episode 1975-1984
Afar rifting episode 2005-2009
Distance along rift segment (km)
80
70
60
50
40
30
20
10
0
−10
−20
1
2
3
4
1975 2005
1976 2006
1977 2007
1978 2008
1979 2009
1980 2010
1981 2011
1982 2012
1983 2013
1984
Year

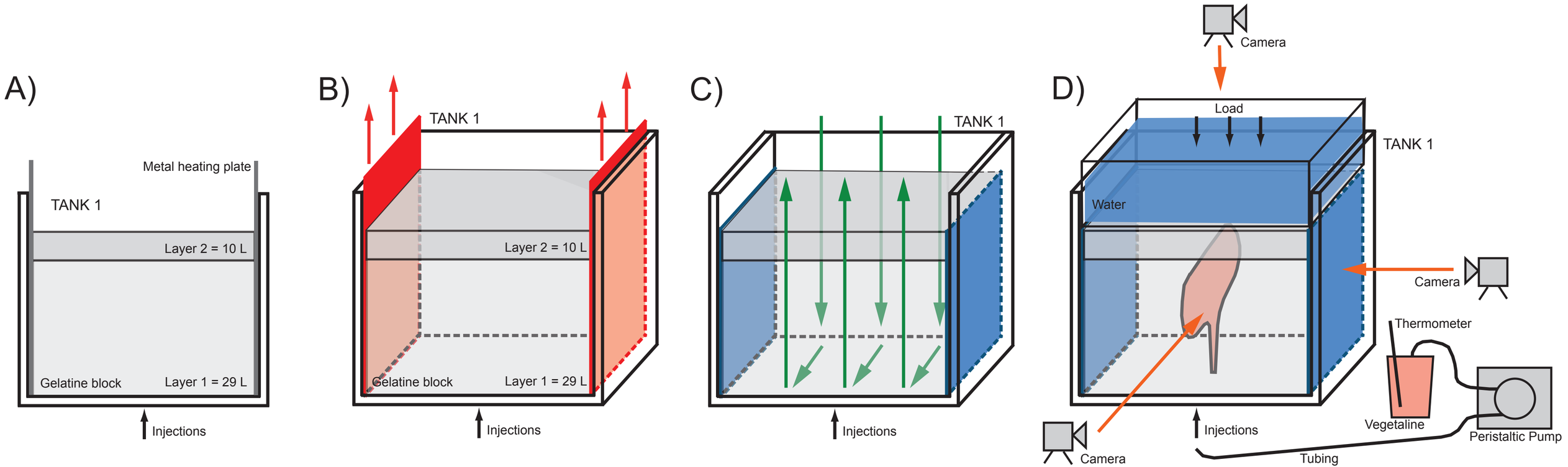
A)
Metal heating plate
TANK 1
Layer 2 = 10 L
Gelatine block
Layer 1 = 29 L
Injections
B)
TANK 1
Layer 2 = 10 L
Gelatine block
Layer 1 = 29 L
Injections
C)
TANK 1
Injections
D)
Camera
Load
TANK 1
Water
Camera
Thermometer
Vegetaline
Peristaltic Pump
Injections
Camera
Tubing

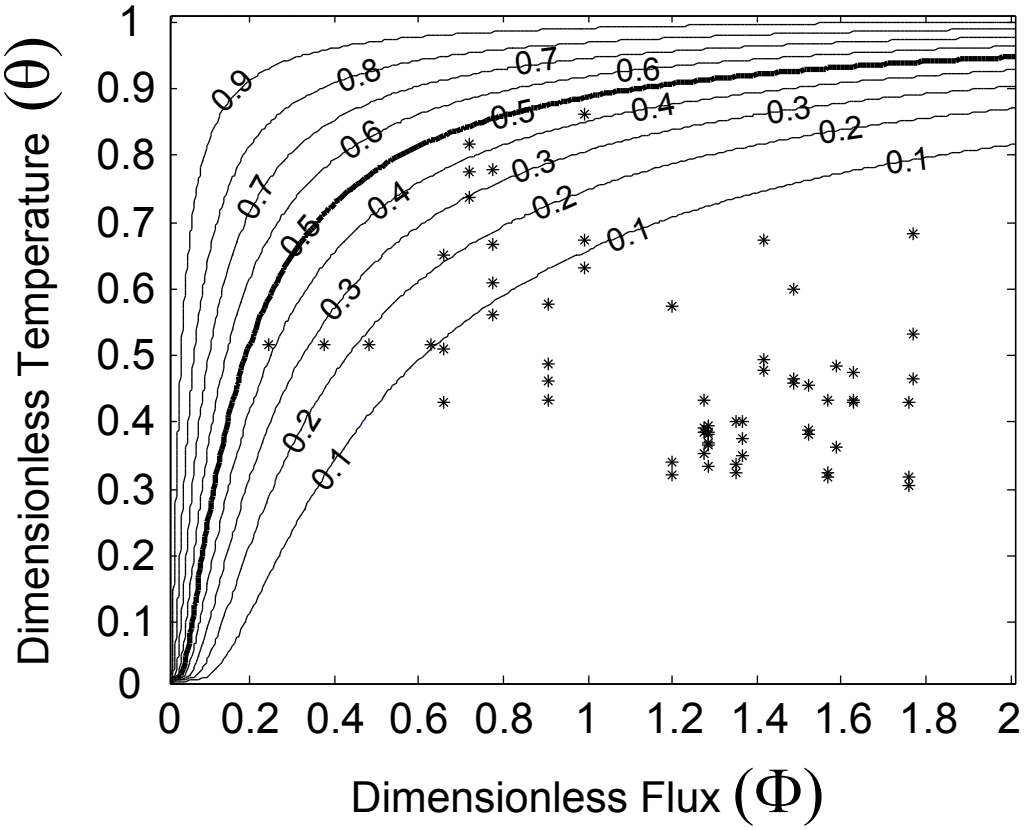
Dimensionless Temperature (θ)
Dimensionless Flux (Φ)
0
0.1
0.2
0.3
0.4
0.5
0.6
0.7
0.8
0.9
1
1.2
1.4
1.6
1.8
2

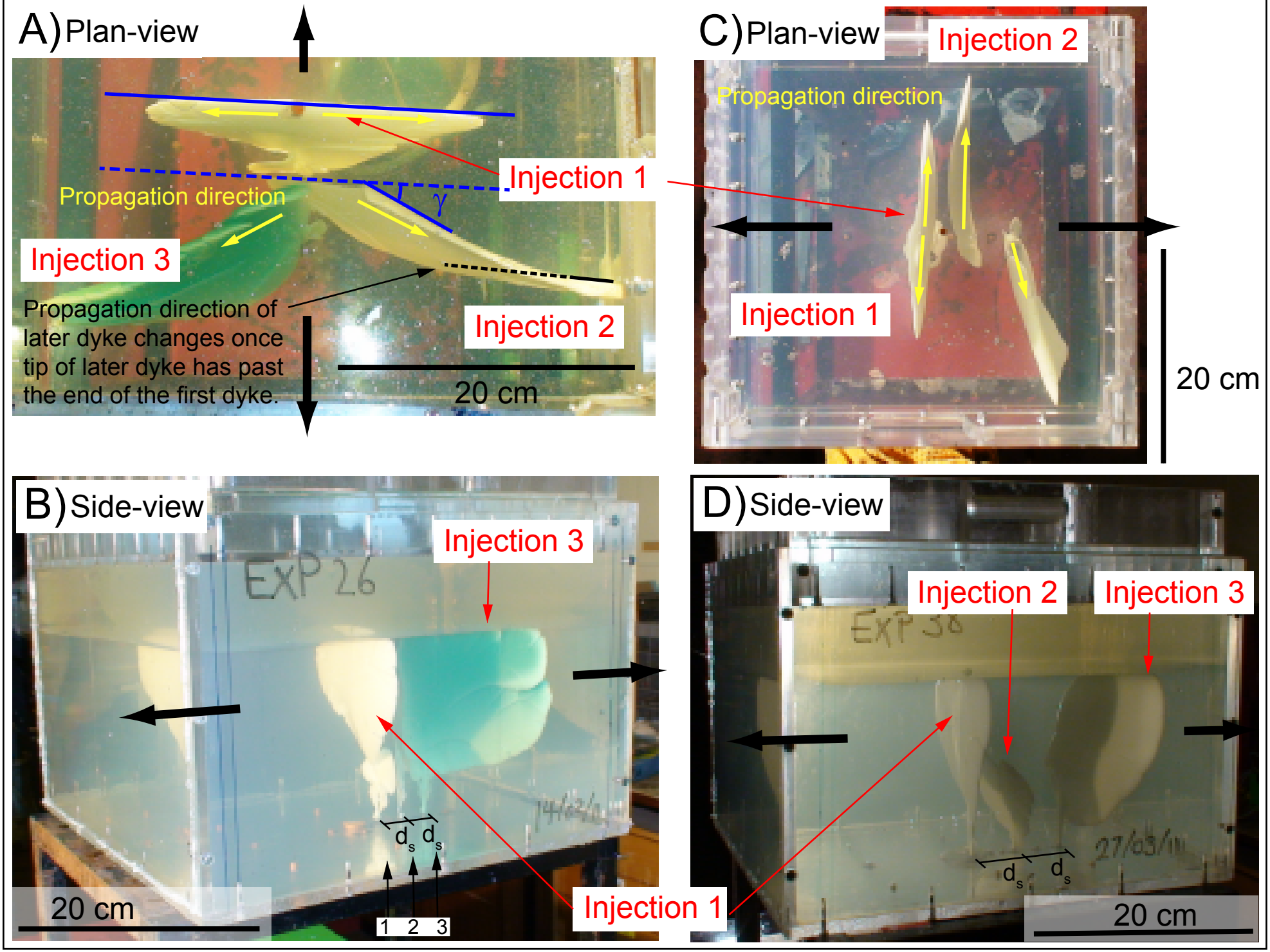
A) Plan-view
Injection 1
Propagation direction
γ
Injection 3
Propagation direction of later dyke changes once tip of later dyke has past the end of the first dyke.
Injection 2
20 cm
C) Plan-view
Injection 2
Propagation direction
Injection 1
20 cm
B) Side-view
Injection 3
EXP 26
Injection 1
d_s d_s
1 2 3
20 cm
D) Side-view
Injection 2
Injection 3
EXP 38
d_s d_s
20 cm

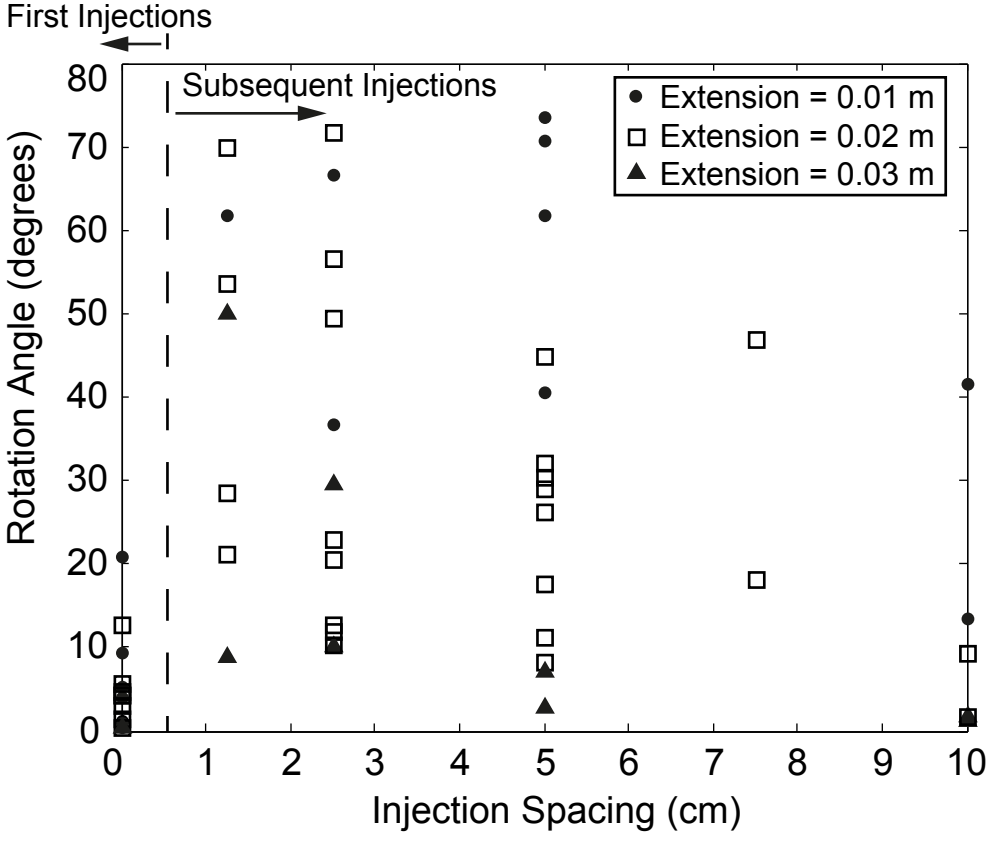
First Injections
Subsequent Injections
Extension = 0.01 m
Extension = 0.02 m
Extension = 0.03 m
Rotation Angle (degrees)
Injection Spacing (cm)
0
10
20
30
40
50
60
70
80
0
1
2
3
4
5
6
7
8
9
10

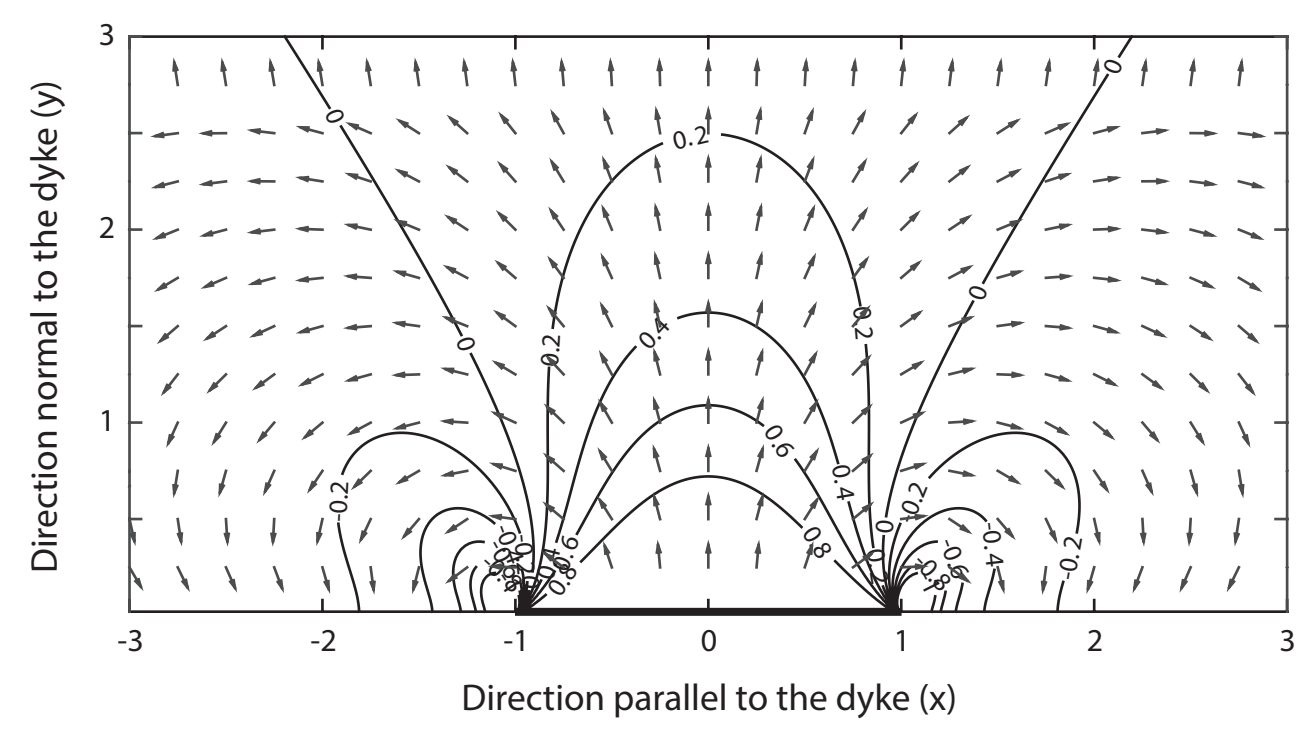
Direction normal to the dyke (y)
Direction parallel to the dyke (x)
3
2
1
-3
-2
-1
0
1
2
3
0
0.2
0.4
0.6
0.8
-0.2
-0.4
-0.6
-0.8

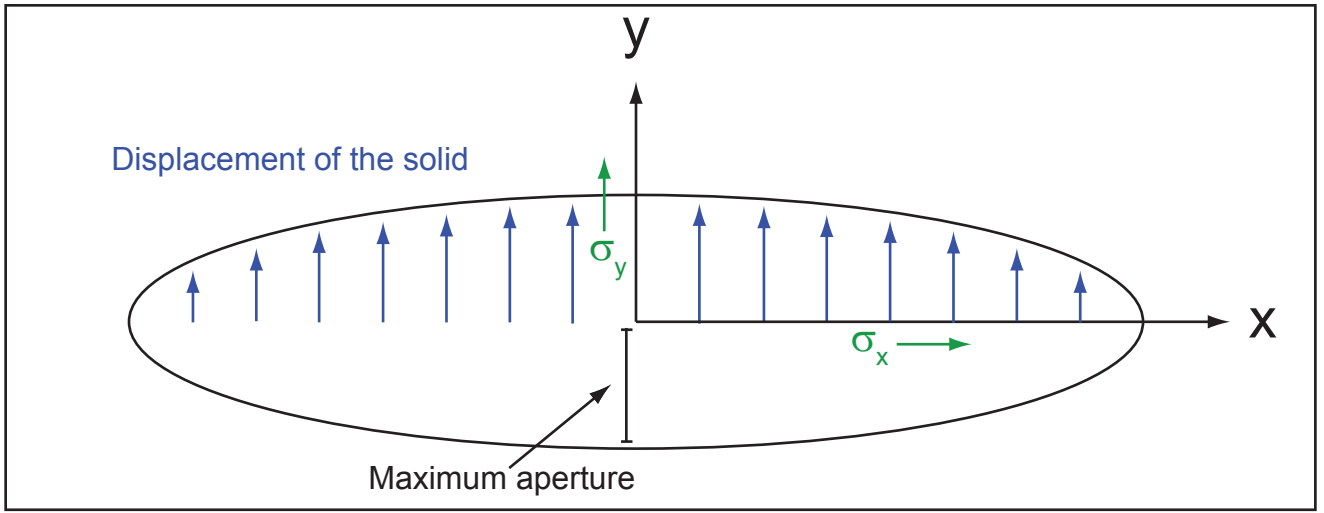
y
Displacement of the solid
σy
σx
x
Maximum aperture

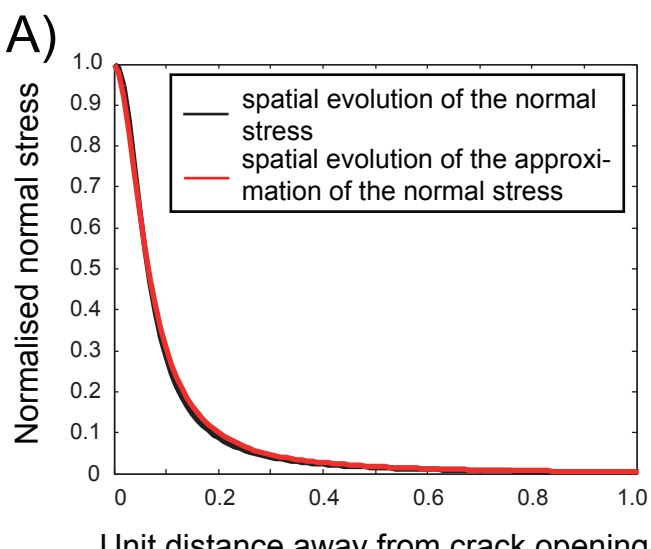
A)
spatial evolution of the normal stress
spatial evolution of the approxi-mation of the normal stress
Normalised normal stress
Unit distance away from crack opening

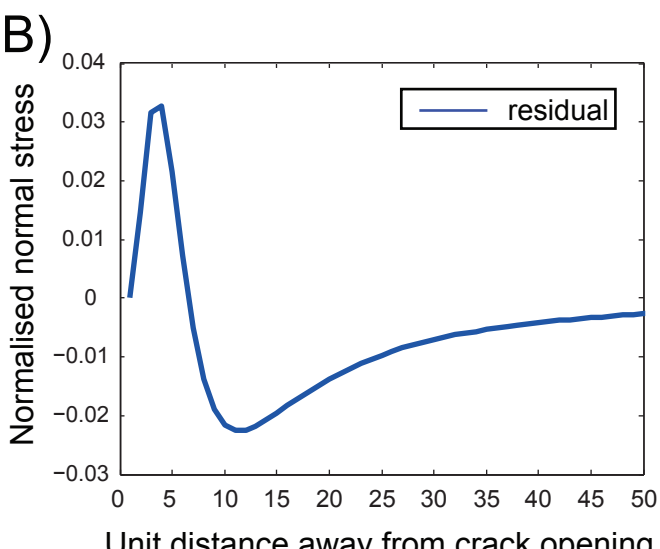
B)
residual
Normalised normal stress
Unit distance away from crack opening

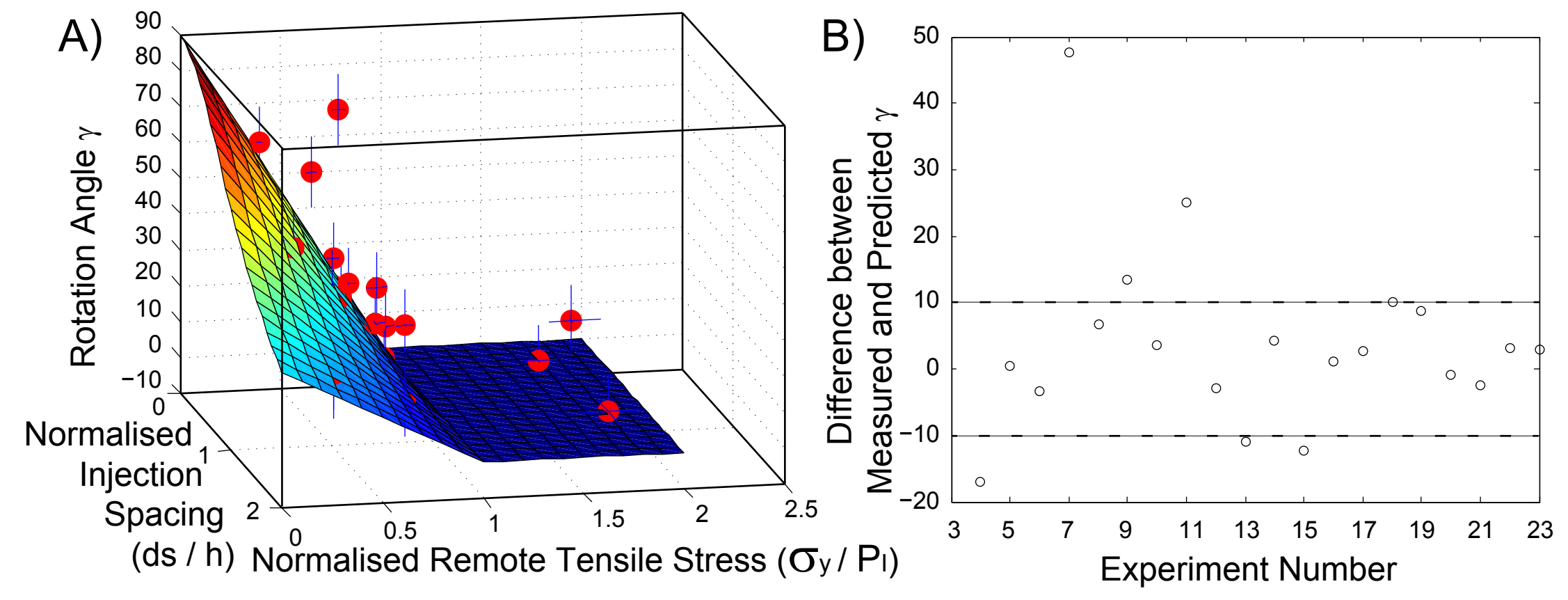
A)
Rotation Angle γ
90
80
70
60
50
40
30
20
10
0
−10
Normalised Injection Spacing (ds / h)
0
1
2
Normalised Remote Tensile Stress (σy / Pl)
0
0.5
1
1.5
2
2.5
B)
Difference between Measured and Predicted γ
50
40
30
20
10
0
−10
−20
3
5
7
9
11
13
15
17
19
21
23
Experiment Number

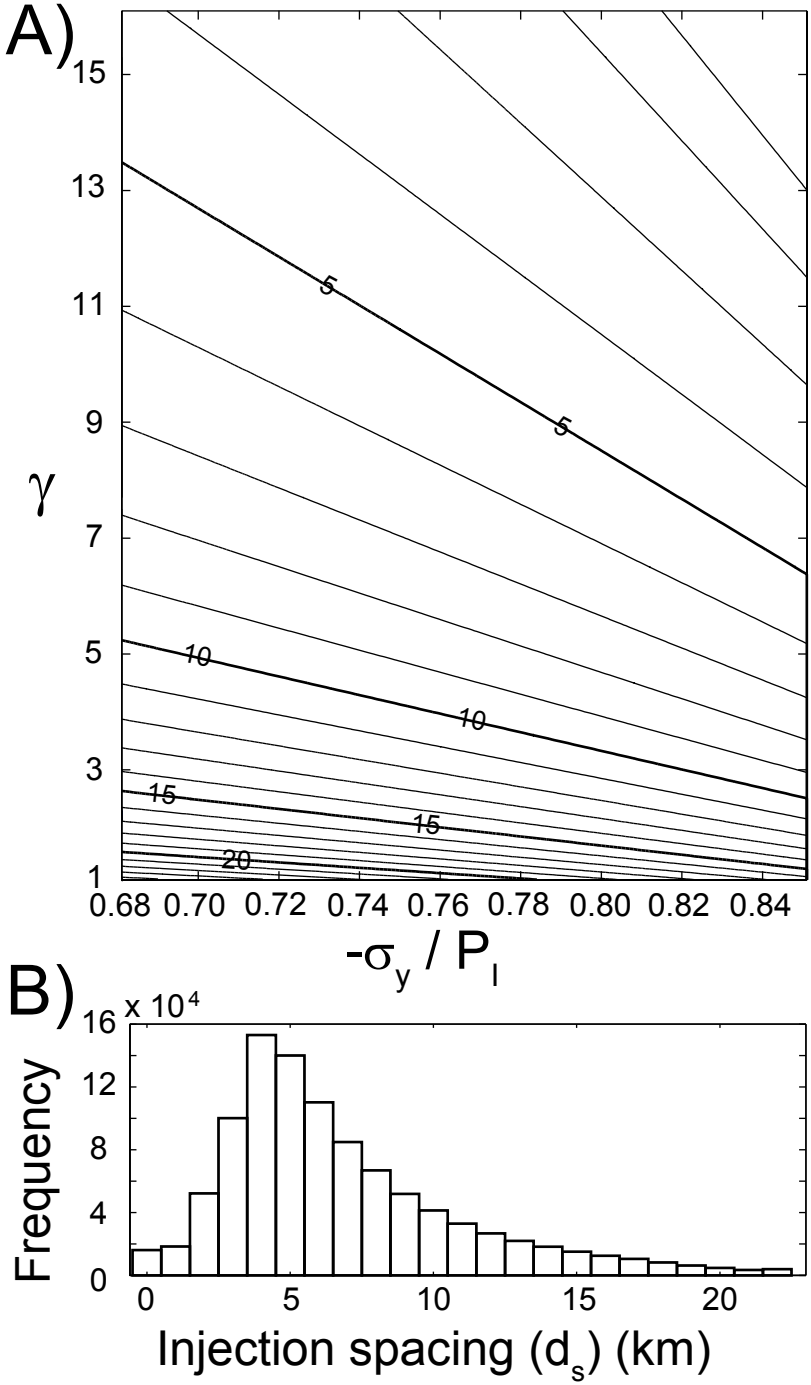
A)
15
13
11
9
7
5
3
1
γ
5
5
10
10
15
15
20
0.68 0.70 0.72 0.74 0.76 0.78 0.80 0.82 0.84
-σy / Pl
B)
x 10^4
16
12
8
4
0
Frequency
0
5
10
15
20
Injection spacing (ds) (km)

Experiment Number	Layer Number	Layer Volume (L)	Gelatine Concentration (wt.%)	Volume Hot Water (L)	Volume Cold Water (L)
1	1	29.6	1.96	12	18
	2	10.36	2.91	6	6
2	1	29.6	1.96	12	18
	2	10.36	2.91	6	6
3	1	29	2	15.87	15
	2	10	5	5.615	5.5
4	1	29	2	15.87	15
	2	10	4	6	5.232
5	1	29	2	15.87	15
	2	10	4	6	5.232
6	1	29	2	15.87	15
	2	10	4	6	5.232
7	1	29	2	15.87	15
	2	10	4	6	5.232
8	1	29	2	15.87	15
	2	10	4	6	5.232
9	1	29	2	15.87	15
	2	10	4	6	5.232
10	1	29	2	15.87	15
	2	10	4	6	5.232
11	1	29	2	15.87	15
	2	10	4	6	5.232
12	1	29	2	15.87	15
	2	10	4	6	5.232
13	1	29	2	15.87	15
	2	10	4	6	5.232
14	1	29	2	15.87	15
	2	10	4	6	5.232
15	1	29	2	15.87	15
	2	10	4	6	5.232
16	1	29	2	15.87	15
	2	10	4	6	5.232
17	1	29	2	15.87	15
	2	10	4	6	5.232
18	1	29	2	15.87	15
	2	10	4	6	5.232
19	1	29	2	15.87	15
	2	10	4	6	5.232
20	1	29	2	15.87	15

	2	10	4	6	5.232
21	1	29	2	15.87	15
	2	10	4	6	5.232
22	1	29	2	15.87	15
	2	10	4	6	5.232
23	1	29	2	15.87	15
	2	10	4	6	5.232

Temperature (^oC)	Soldification Time (mins)	Cold room Temperature (^oC)	Young's Modulus E	Gelatine Extension (mm)	Surface Load (kgs)	Tensile Stress s_x (Pa)
unknown	1470	4	3064	0	no load	0
unknown	485	4	3156	0	no load	0
unknown	1040	4	2381	~20	7	169
unknown	350	4	2763	~20	7	169
unknown	1161	4	4697	~20	8	334
unknown	395	4	7333	~20	8	334
33.5	1215	4	1830	~20	8	130
33.5	550	4	4084	~20	8	130
41	1240	4	1602	20	5	114
37	365	4	2835	20	5	114
36.5	1060	4	1270	20	12	90
37.5	365	4	1908	20	12	90
42.5	1104	4	1484	20	6.32	105
37	369	4	2738	20	6.32	105
42.5	1115	4	1303	20	5.5	93
37	335	4	2522	20	5.5	93
44	1400	4	2327	20	6	165
34	310	4	2838	20	6	165
41.5	1230	4	1549	20	6	110
37	355	4	3242	20	6	110
37	1245	4	1750	10	3.5	62
37	323	4	2818	10	3.5	62
41.5	1365	4	1921	10	3.5	68
34	643	4	5062	10	3.5	68
42.5	1400	4	1627	10	3	58
34	325	4	2811	10	3	58
43.5	1515	4	1809	10	4	64
35.5	560	4	4154	10	4	64
42.5	1390	4	1791	10	4	64
38.5	590	4	5563	10	4	64
37	1400	4	1961	30	9.25	209
36	560	4	4322	30	9.25	209
40	1365	4	2561	30	8	273
31	315	4	3999	30	8	273
40	1350	4	2202	30	8	235
28	405	4	5010	30	8	235
40.5	1330	4	1891	30	7.5	201
31.5	495	4	5726	30	7.5	201
42.5	1380	4	1767	20	5	125

30	750	4	6775	20	5	125
42	1460	4	2245	20	6.25	159
24.5	370	4	4273	20	6.25	159
43.5	1395	4	1814	20	6.75	129
26	485	4	5548	20	6.75	129
39	1397	4	2109	20	6.25	150
33.5	792	4	5963	20	6.25	150

Experiment Number	Injection Number	Gelatine Temperature (°C)	Starting Injection Temperature (°C)	Finishing Injection Temperature (°C)
1	1	unknown	50-60	unknown
	2	unknown	50-60	unknown
	3	unknown	50-60	unknown
2	1	unknown	50-60	unknown
	2	unknown	50-60	unknown
3	1	unknown	50-60	unknown
	2	unknown	50-60	unknown
4	1	unknown	50-60	unknown
	2	unknown	50-60	unknown
	3	unknown	50-60	unknown
5	1	unknown	40	31
	2	unknown	42	41
	3	unknown	38	37
6	1	21.5	42	28
	2	21.5	43.5	unknown
	3	21.5	41	unknown
	4	21.5	38	unknown
7	1	17	42	35
	2	17	unknown	40
	3	17	38	36
	4	17	35	32
8	1	18	42.5	40
	2	18	46	45
	3	18	37	unknown
9	1	unknown	46	39.5
	2	unknown	36	33.5
	3	unknown	49	42
10	1	17.5	47	36
	2	17.5	46.5	41
	3	17.5	40	39.5
11	1	19	47	42.5
	2	19	42.5	40
	3	19	37.5	35
12	1	15.5	61	48
	2	15.5	64	52
	3	15.5	42.5	unknown
13	1	13.5	49	30
	2	13.5	50	unknown
	3	13.5	39.5	unknown
14	1	13.5	58	40
	2	13.5	63	60
	3	13.5	59	59
	4	13.5	54	52.5

15	1	14	58.5	45
	2	14	65	59
	3	14	58	50
16	1	12.5	70.5	55
	2	12.5	73	65
	3	12.5	55.5	50
17	1	13	68.5	61
	2	13	66.5	63.5
	3	13	58	56
18	1	13	69.5	64.5
	2	13	68.5	47
	3	13	54.5	53
19	1	15	57	51
	2	15	56	52
	3	15	50	46
20	1	13	55	50
	2	13	54.5	51
	3	13	51	45
21	1	13	61.5	59.5
	2	13	58.5	53
	3	13	62	58
22	1	14	61	unknown
	2	14	61	54.5
	3	14	49	44.5
23	1	13.5	60	54
	2	13.5	63.5	59
	3	13.5	57	48

Injection Spacing d_s (m)	Injection Flow-Rate (rpm)	Injection Flow-Rate (ml/min)	Injection Time (s)	Volume (ml)	Injection Orientation γ (^{o})	Description
0	10	59.8	322	321	1.1	
0.05	10	59.8	442	440	7.7	1st and 2nd
0.075	10	59.8	56	56	unknown	
0	10	59.8	245	244	5.9	
0.025	10	59.8	271	270	10.1	1st and 2nd
0	10	59.8	503	501	unknown	
0.025	10	59.8			unknown	
0	10	59.8	230	229	4.6	
0.05	10	59.8	382	381	11.0	1st and 2nd
0.075	10	59.8	357	356	18.1	2nd and 3rd
0	10	59.8	357	356	12.8	
0.05	10	59.8	225	224	30.3	1st and 2nd
0.05	10	59.8	223	222	44.9	1st and 3rd
0	10	59.8	317	316	3.1	
0.025	10	59.8	170	169	20.7	1st and 2nd
0.025	10	59.8	128	128	71.6	2nd and 3rd
0.025	10	59.8	125	125	11.7	3rd and 4th
0	10	59.8	368	367	0.3	
0.0125	10	59.8	130	130	69.9	1st and 2nd
0.05	10	59.8	192	191	26.1	1st and 3rd
0.075	10	59.8	193	192	47.0	3rd and 4th
0	20	119.6	135	269	4.2	
0.05	20	119.6	132	263	17.6	1st and 2nd
0.05	20	119.6	111	221	32.1	1st and 3rd
0	20	119.6	126	251	3.6	
0.025	20	119.6	84	167	22.9	1st and 2nd
0.025	20	119.6	102	203	56.7	2nd and 3rd
0	20	119.6	169	337	1.5	
0.0125	20	119.6	94	187	28.6	1st and 2nd
0.0125	20	119.6	31	62	unknown	
0	10	59.8	219	218	20.8	
0.05	10	59.8	234	233	61.8	1st and 2nd
0.05	10	59.8	100	100	73.4	2nd and 3rd
0	20	119.6			9.4	
0.05	20	119.6			40.6	1st and 2nd
0.05	20	119.6			70.7	2nd and 3rd
0	20	119.6			3.8	
0.025	20	119.6			36.8	1st and 2nd
0.025	20	119.6			66.5	2nd and 3rd
0	20	119.6	215	428	5.3	
0.0125	20	119.6	37	74	61.8	1st and 2nd
0.0125	20	119.6	22	44		
0.05	20	119.6	86	171		

0	20	119.6	230	458	1.0	
0.1	20	119.6	192	383	13.4	1st and 2nd
0.1	20	119.6	142	283	41.6	2nd and 3rd
0	30	179.4	196	586	0.3	
0.1	30	179.4	117	350	1.0	1st and 2nd
0.1	30	179.4	142	424	1.7	2nd and 3rd
0	30	179.4	114	341	0.3	
0.05	30	179.4	113	338	2.7	1st and 2nd
0.05	30	179.4	100	299	7.1	2nd and 3rd
0	30	179.4	91	272	0.4	
0.025	30	179.4	60	179	10.0	1st and 2nd
0.025	30	179.4	55	164	29.6	2nd and 3rd
0	25	149.5	118	294	0.4	
0.0125	25	149.5	77	192	8.7	1st and 2nd
0.0125	25	149.5	65	162	50.0	2nd and 3rd
0	25	149.5	132	329	4.6	
0.1	25	149.5	178	443	9.4	1st and 2nd
0.1	25	149.5	124	309	1.6	2nd and 3rd
0	25	149.5	123	306	3.6	
0.05	25	149.5	59	147	8.4	1st and 2nd
0.05	25	149.5	109	272	28.7	2nd and 3rd
0	25	149.5	172	428	3.3	
0.025	25	149.5	114	284	12.8	1st and 2nd
0.025	25	149.5	159	396	49.5	2nd and 3rd
0	25	149.5	131	326	0.0	
0.0125	25	149.5	63	157	21.2	1st and 2nd
0.0125	25	149.5	67	167	53.6	2nd and 3rd

Injection Thickness (m)	Dimensionless Temperature Θ	Dimensionless Flux Φ	α
0.024	0.517	0.376	0.26431
0.020	0.517	0.376	0.26431
unknown	0.517	0.376	0.26431
0.016	0.517	0.484	0.18037
0.016	0.517	0.484	0.18037
unknown	0.517	0.245	0.41972
unknown	0.517	0.245	0.41972
0.020	0.517	0.630	0.10772
0.016	0.517	0.630	0.10772
0.020	0.517	0.630	0.10772
0.026	0.775	0.719	0.37442
0.012	0.738	0.719	0.31024
0.020	0.816	0.719	0.45626
0.021	0.463	0.907	0.02380
0.008	0.432	0.907	0.01688
unknown	0.487	0.907	0.03034
unknown	0.576	0.907	0.06834
0.023	0.560	0.776	0.08958
0.014	0.609	0.776	0.12674
0.014	0.667	0.776	0.18505
0.013	0.778	0.776	0.35144
0.018	0.531	1.768	0.00247
0.015	0.464	1.768	0.00070
0.018	0.684	1.768	0.02744
0.017	0.674	0.990	0.12311
0.009	0.861	0.990	0.45218
0.012	0.633	0.990	0.08803
0.021	0.458	1.487	0.00197
0.009	0.466	1.487	0.00226
unknown	0.600	1.487	0.01705
0.016	0.429	0.658	0.05033
0.015	0.511	0.658	0.09339
0.010	0.649	0.658	0.21717
0.020	0.341	1.200	0.00098
0.017	0.320	1.200	0.00065
0.016	0.574	1.200	0.02819
0.019	0.493	1.416	0.00465
0.004	0.479	1.416	0.00377
0.004	0.673	1.416	0.04950
0.023	0.393	1.274	0.00171
unknown	0.354	1.274	0.00083
unknown	0.385	1.274	0.00147
0.002	0.432	1.274	0.00325

0.019	0.382	1.287	0.00131
0.018	0.333	1.287	0.00051
0.015	0.386	1.287	0.00142
0.014	0.319	1.762	0.00002
0.012	0.306	1.762	0.00001
0.016	0.430	1.762	0.00035
0.019	0.324	1.349	0.00029
0.021	0.336	1.349	0.00038
0.019	0.400	1.349	0.00132
0.015	0.319	1.569	0.00007
0.011	0.324	1.569	0.00008
0.021	0.434	1.569	0.00089
0.022	0.381	1.523	0.00038
unknown	0.390	1.523	0.00046
0.012	0.457	1.523	0.00168
0.019	0.429	1.630	0.00061
0.008	0.434	1.630	0.00068
0.016	0.474	1.630	0.00146
0.019	0.371	1.283	0.00110
0.012	0.396	1.283	0.00170
0.014	0.367	1.283	0.00102
0.017	0.362	1.587	0.00017
0.011	0.486	1.587	0.00215
0.009	0.486	1.587	0.00215
0.021	0.376	1.366	0.00078
unknown	0.350	1.366	0.00046
unknown	0.402	1.366	0.00127

Comments

Reached Surface
Reached Surface
Reached Surface
Reached Surface
Reached Surface

Reached Surface

Unrecorded
Reached Surface

Unrecorded
Merged
Some migration into top layer
Merged and Reached Suface

Unrecorded

Merged

Merged
Merged
Reached Surface

Experiment Number	Injection Number	Young's Modulus E	Crack Aperture (m)	Crack Half-height h (m)	Calculated Overpressure (Pa)
1	1	3064.331	0.0238	unknown	unknown
	2	3064.331	0.01973	unknown	unknown
	3	3064.331	unknown	unknown	unknown
2	1	2380.685	0.0158	unknown	unknown
	2	2380.685	0.0155	unknown	unknown
3	1	4696.673	unknown	0.069	unknown
	2	4696.673	unknown	unknown	unknown
4	1	1829.971	0.02031	0.047	264
	2	1829.971	0.01585	0.061	158
	3	1829.971	0.02031	unknown	unknown
5	1	1602.127	0.02579	0.069	200
	2	1602.127	0.01171	unknown	unknown
	3	1602.127	0.01953	unknown	unknown
6	1	1270.435	0.02143	0.072	126
	2	1270.435	0.00798	0.061	55
	3	1270.435	unknown	unknown	unknown
	4	1270.435	unknown	unknown	unknown
7	1	1483.977	0.02263	0.08	140
	2	1483.977	0.01437	unknown	unknown
	3	1483.977	0.01378	0.074	92
	4	1483.977	0.01314	unknown	unknown
8	1	1303.354	0.01821	0.073	109
	2	1303.354	0.01498	0.080	81
	3	1303.354	0.01756	0.069	111
9	1	2326.723	0.01675	0.07	186
	2	2326.723	0.00875	0.07	97
	3	2326.723	0.0115	0.07	127
10	1	1549.33	0.0209	0.070	153
	2	1549.33	0.00939	0.066	73
	3	1549.33	unknown	unknown	unknown
11	1	1750.309	0.01571	0.07	131
	2	1750.309	0.01469	0.07	122
	3	1750.309	0.01021	0.07	85
12	1	1920.55	0.0198	0.072	177
	2	1920.55	0.01652	0.064	165
	3	1920.55	0.01648	0.078	135
13	1	1626.57	0.01913	0.079	131
	2	1626.57	0.00392	0.067	32
	3	1626.57	0.0037	0.071	28
14	1	1808.946	0.02309	0.076	182
	2	1808.946	unknown	unknown	unknown
	3	1808.946	unknown	unknown	unknown
	4	1808.946	0.0016	0.04	24

15	1	1790.507	0.01875	0.074	152
	2	1790.507	0.01764	0.065	162
	3	1790.507	0.01541	0.067	137
16	1	1961.181	0.0135	0.076	116
	2	1961.181	0.01213	0.050	159
	3	1961.181	0.01614	0.074	143
17	1	2561.393	0.0194	0.101	164
	2	2561.393	0.021	0.100	179
	3	2561.393	0.01908	0.057	286
18	1	2202.35	0.01458	0.086	125
	2	2202.35	0.01077	0.078	101
	3	2202.35	0.02115	0.071	219
19	1	1891.032	0.02225	0.075	187
	2	1891.032	unknown	0.053	unknown
	3	1891.032	0.01168	0.044	167
20	1	1766.946	0.01935	0.067	169
	2	1766.946	0.0075	0.061	72
	3	1766.946	0.01571	0.067	138
21	1	2244.73	0.01893	0.076	187
	2	2244.73	0.01189	0.063	142
	3	2244.73	0.01441	0.080	135
22	1	1814.446	0.01732	0.072	145
	2	1814.446	0.01083	0.056	117
	3	1814.446	0.00949	0.020	294
23	1	2108.624	0.0205	0.077	188
	2	2108.624	unknown	0.068	unknown
	3	2108.624	unknown	0.052	unknown

Applied Remote Tensile Stress (Pa)
unknown
-169
-334
-130
-114
-90
-105
-93
-165
-110
-62
-68
-58
-64

-64

-209

-273

-235

-201

-125

-159

-129

-150